INVESTIGATION OF NONLINEAR DAMPING IN VIBRATION ENERGY HARVESTERS

by

Asil Arif Aksekili

Submitted to the Institute of Graduate Studies in
Science and Engineering in partial fulfilment of
the requirements for the degree of
Master of Science
in
Mechanical Engineering

Yeditepe University
2013

INVESTIGATION OF NONLINEAR DAMPING IN VIBRATION ENERGY
HARVESTERS

APPROVED BY:

Asst. Prof. Dr. Nezih TOPALOĞLU   ……………………………………
(Thesis Supervisor)

Asst. Prof. Dr. Namık CIBLAK   ……………………………………

Prof. Dr. Abdülkerim KAR   ……………………………………

DATE OF APPROVAL: 23/09/2013

ACKNOWLEDGEMENTS

ABSTRACT

INVESTIGATION OF NONLINEAR DAMPING IN VIBRATION ENERGY HARVESTERS

Energy harvesting continually attracts more interest as a result of the development technologies such as wireless sensor network systems, condition-based monitoring (CBM) applications, structural monitoring systems, etc. Although there are many sources in the nature that can be used as ambient energy source like solar energy, wind energy and thermal energy, vibration based energy harvesters outshines among them because of its abundance and non-availability of solar energy every time. In a conventional vibration energy harvester with electromagnetic transduction mechanism, the electrical damping is linear. Because of some design challenges like limited travel span for the proof mass of the system and variable ambient vibration characteristics, many suggestions are offered up to now in order to increase the efficiency of these harvesters. Within this scope, in this study, using nonlinear electrical damping is proposed. In order to compare the efficiencies of the linearly and nonlinearly damped systems, they are both modelled and solved numerically in MATLAB environment. The simulations are carried on for both with and without including parasitic damping. Over a range of ambient vibration amplitudes and frequencies, power results are normalized and comparisons are made. It is seen that using nonlinear damping increases efficiency of the harvester in majority of the testing range when parasitic damping is not included in the analysis. As the nonlinearity of the damping increases, the efficiency of the system increases as well. When the effect of parasitic damping is examined, it is seen that as the amount of parasitic damping increases, the superiority of the nonlinear damping decreases. For the second part of the study, nonlinear damping is realized physically. An experimental setup that can hold five different coil loops and measure the open circuit voltages is design and built. For the experimental study, firstly, the relationships of the effect of magnet speed and coil turn numbers are established with initial experiments. After that an algorithm is written to calculate the desired coil configuration for a desired damping profile. The required configuration is calculated with DPF and tested experimentally with two different damping profiles one representing linear

and other representing the nonlinear case. It is seen that the written algorithm successfully calculates the linear and nonlinear damping profiles. The results are then validated experimentally. As a result of this study, it is shown that nonlinear damping can be an effective and applicable way to increase the efficiencies of the vibration based energy harvesters in the future.

ÖZET

DOĞRUSAL OLMAYAN SÖNÜMLEMENİN ENERJİ ÜRETEÇLERİ ÜZERİNDEKİ ETKİSİNİN İNCELENMESİ

Enerji üreteçlerinin önemi kablosuz sensör ağı sistemleri, durum görüntüleme (CBM) uygulamaları, yapısal kontrol sistemleri gibi teknolojilerin gelişmesiyle günden güne artmaktadır. Doğada güneş enerjisi, rüzgar enerjisi, termal enerji gibi enerji üretimi için kullanılabilecek farklı kaynaklar olmasına rağmen titreşimden enerji üretmek bu enerji kaynağının çokluğu ve güneş enerjisinin her zaman ve her yerde bulunmamasından dolayı gün geçtikçe daha çok ön plana çıkmaktadır. Geleneksel bir titreşim tabanlı, elektromanyetik çevrim mekanizmasına sahip enerji üretecinde elektriksel sönümleme doğrusaldır. Sistem içindeki hareketli kütlenin sınırlı hareket alanı olması ve değişken dış ortam titreşim karakteristikleri gibi tasarım zorluklarından dolayı bu üreteçlerin verimlerinin arttırılması için bugüne kadar yapılmış çeşitli çalışmalar mevcuttur. Bu tezde sunulan çalışmada söz konusu üreteçler için doğrusal olmayan elektriksel sönümleme kullanılması önerilmektedir. Doğrusal ve doğrusal olmayan elektriksel sönümlemelerin karşılaştırılabilmesi için sistemler modellenerek MATLAB ortamında nümerik olarak çözdürülmüştür. Simülasyonlar parazitik sönümlemenin olduğu ve olmadığı iki farlı durum için yapılmıştır. Simülasyonlardan verilmiş ortam titreşim frekansı ve genliği aralıkları için alınan sonuçlar normalize edilerek farklı durumlar birbirleriyle karşılaştırılmıştır. Sonuçlara bakıldığında parazitik sönümlemenin olmadığı durumlarda doğrusal olmayan sönümlemenin uygulandığı sistem doğrusal sönümlenin uygulandığı sisteme göre test uzayının genelinde daha verimli sonuç vermiştir. Doğrusal olmayan sönümlemenin derecesi arttıkça sistemin daha verimli hale geldiği görülmüştür. Parazitik sönümlemenin sistem üzerindeki etkisi incelendiğinde sistem parazitik sönümleme değeri arttıkça doğrusal olmayan elektriksel sönümleden alınan verim artışının azaldığı görülmüştür. Çalışmanın ikinci bölümünde doğrusal olmayan elektriksel sönümleme fiziksel olarak oluşturulmaya çalışılmıştır. Birbirinden bağımsız beş ayrı sarım bölgesi olan ve zamana bağlı açık devre voltajlarının ölçülebildiği bir deney düzeneği tasarlanmış ve üretilmiştir.

Deney çalışmasında ilk olarak mıknatıs hızı ve sarım sayılarının üretilen voltaj üzerindeki etkisi incelenmiştir. Daha sonra ilk deneylerden alınan sonuçlar kullanılarak istenen sönümleme profilini elde etmek için kullanılması gereken sarım konfigurasyonunu belirleyebilmek adına bir kod yazılmıştır. Yazılan kod ile doğrusal ve doğrusal olmayan iki farklı sönümleme profili için gerekli sarım konfigürasyonları hesaplanmış ve deneysel olarak test edilmiştir. Sonuçlara bakıldığında hazırlanan algoritmanın gerekli sarım konfigürasyonunu başarı ile hesaplayabildiği ve deneysel olarak doğrulanabildiği görülmüştür. Sonuç olarak bu çalışmada enerji üreteçleri için doğrusal olmayan elektriksel sönümlemenin uygulanabilir ve verimi arttıran bir metod olduğu gösterilmiştir.

TABLE OF CONTENTS

LIST OF FIGURES

LIST OF TABLES

LIST OF SYMBOLS / ABBREVIATIONS

$MEMS$	Micro electro mechanical systems
CBM	Condition based monitoring
PM	Proof mass
DPF	Damping profile finder
$DCOS$	Damping constant optimization subfunction
RPM	Revolution per minute
ω	Vibration frequency (rad/s)
ω_n	Natural frequency (rad/s)
k	Spring constant (N/m)
y	Frame displacement (m)
z	Relative displacement of the proof mass (m)
Z_l	Boundary location (m)
D	Electrical damping constant
D_p	Parasitic damping constant
ζ_p	Parasitic damping ratio
P^*	Nondimensionalized power

1. INTRODUCTION

There have been many inventions and discoveries that can be accounted as the "key stones" of our current technological level throughout the history of humanity. Among all of them, discovery of electricity outshines obviously since it enabled the development of almost all systems and devices that we use currently. Electricity is the main source of power for today's world. Up to some point, it has been produced and served to people by different kinds of electricity production facilities.

Any device that operates with electricity had to be connected to an electricity power source by means of cables and wires. When the new developments required to get rid of these connection tools, engineers and scientists developed electricity storage system as we are now calling them "batteries". They worked and still working very well for the systems that require being wireless, but the main problem of them is that they require to be re-charged after a certain period of time. To be able to solve the dependency of electrical devices to electricity power sources, various solutions have been emerged up to now. The most accepted solution is to generate electricity within the system where it is going to be used. At this stage, the idea of "energy harvesting" is born.

The definition of energy harvesting as Wikipedia suggests is as follows: "Energy harvesting (also known as power harvesting or energy scavenging) is the process by which energy is derived from external sources, captured and stored for small, wireless autonomous devices, like those used in wearable electronics and wireless sensor networks". The devices designed for energy harvesting purpose are called "energy harvesters".

The increasing usage of systems that use small amount of energy and operate autonomously provides encouragement to researches in the field of energy harvesting. The wireless network systems and condition-based monitoring (CBM) applications [1] that are being used for structural health monitoring of various machines can be considered as the most well known areas that require energy harvesters [2]. There are also some known application areas in the literature, such as inside of commonly used household devices like

washing machines, to power up some integrated sensors by using the vibration sourced by rotating unbalance [3]. Energy harvesters can be used in these applications by one of two ways; either increasing the battery life of the system or provide all required power that they need.

All example applications mentioned above require small amount of power. Although designing and building an energy harvester can be done in bulk scale, since design specifications of these common application areas require them to be relatively small, an important portion of the research that have been done up to now is mainly focused on MEMS (Micro Electro Mechanical Systems) scale energy harvesters.

There are varieties of energy sources in nature that can be used by energy harvesters to be converted into electricity. The most commonly used ones can be listed as follows:

- Solar energy
- Wind energy
- Thermal energy
- Vibration energy

Many different and successful kinds of designs that have been made can be found in literature. All ambient energy sources have different pros and cons when they are compared. Although solar energy appeared to be the solution for most of the designs, vibration energy outshines in the last years due to its abundance and non-availability of solar energy in everywhere and every time of the day [4]. The main focus of this thesis work can be classified as suggesting different approaches to the design stage of vibration based energy harvesters.

1.1. VIBRATION BASED ENERGY HARVESTING

The principle of vibration based energy harvesting can be summarized as using mechanical vibration as an ambient energy source and converting it into electricity by means of a mechanical-to-electrical transducer. Several different design approaches have been suggested in the past few years. They can be categorized into three main types considering

the transduction mechanism they use to extract electricity from vibration. These mechanisms can be listed as piezoelectric, electrostatic and electromagnetic systems [5]. There are also other mechanisms recently proposed, such as magnetostrictive systems but they need further development to be considered as an energy harvester mechanism.

Piezoelectric systems use the features of piezo-materials. This special type of material produces electricity when deformed by an external force. In other words, mechanical strain can be converted into electrical voltage and current. They are commonly used inside a harvester as a piezo layer on top of a cantilever beam. In that configuration, electricity is extracted from the piezo-layer while the beam is vibrated externally (Figure 1.1).
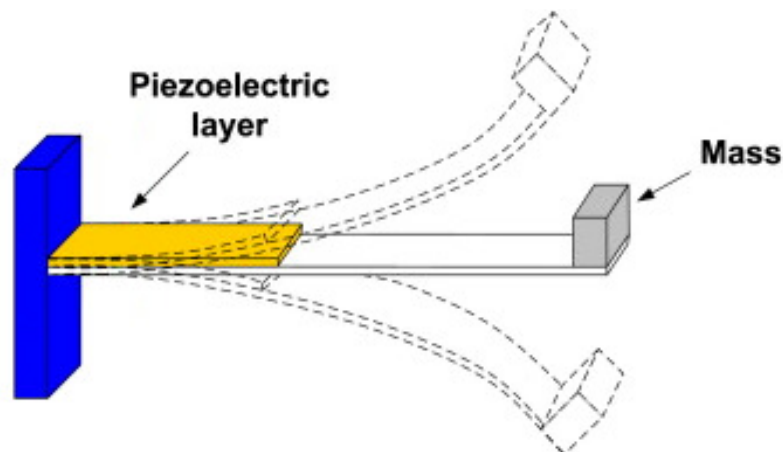
Figure 1.1. Piezoelectric beam example

The ambient vibration source for these devices can be anything from footsteps of a human to acoustic waves. A successful and commercially available example of this application is a batteryless remote control being produced by Philips company (Figure 1.2). This device can produce its own electricity by the help of a self contained piezo based harvester that gets its power from the hand movements of the user.

Figure 1.2. Batteryless remote control by Philips

Another type of energy harvesters is electrostatic (also known as capacitive) type. These harvesters work with the principle of changing the distance between the plates of a charged capacitor. The movement of the charged plates can be obtained by means of an external vibration source and electricity can be extracted.

Finally, harvesters with electromagnetic transduction mechanisms use the principle called Faraday's Law of magnetic induction which can be described briefly as; if you move a magnet back and forth within the vicinity of some coil loops, you will be able to have potential difference between the two ends of the conducting wires making the coil loops. This potential difference is equal to the rate of change of the magnetic flux passing through the coil loops. A well known energy harvester example that works on this principle is the commercially available handshake flashlight (Figure 1.3). It contains a moving magnet and coil loops inside of a tube. As the user shakes the flashlight, electricity is being produced and stored into a battery for later use.

Figure 1.3. Handshake flashlight

All of these three transduction mechanisms are popular due to their good compatibility with MEMS systems and production techniques [5]. Among these mechanisms, the focus of this thesis is using electromagnetic principles to extract electricity from vibrating environment.

1.2. PROBLEM DEFINITION

Up to now, researches designing an electromagnetic based vibration energy harvester in micro scale state that there are some unique difficulties. Some of the major and still worth of further research ones are described below.

The first major problem comes from the nature of the vibrating source. Most of the vibration sources in the nature have variable frequency range meaning that the excitation frequency of the environment may change over time. This variation may be in the form of a periodic change or it even can be a random change. However, most of the harvesters designed up to now give their best performance when the frequency of ambient vibration, ω, is close to the natural frequency, ω_n, of the designed device. In other words, the efficiency of the harvester is maximum when the system operates at its resonant frequency ($\omega/\omega_n \approx 1$) [2]. As a result, the efficiencies of harvester is linked by the nature of the ambient vibration.

Another major problem comes from the dimension requirements. For an energy harvester, the distance provided to the proof mass of the device to allow it to move back and forth during operation is limited. This problem is more severe in MEMS scale. The maximum distance that could be provided for a MEMS device is reported as 0.9 mm [6]. The unwanted collusion of the proof mass with boundaries would cause an energy loss and decrement in the efficiency of the system. To solve this problem, an appropriate electrical damping constant should be selected for the harvester to slow the proof mass down but again this is another source of loss for the efficiency of the system.

These are the two main challenges for the design stage of a highly efficient energy harvester and still draws quite amount of interests of the researchers all around the world. The common approaches on solving them are mentioned in Section 1.3 in detail.

1.3. LITERATURE SURVEY

There are several studies in the literature that came up with different approaches to solve the design challenges mentioned in the previous section. Among them, the major and mostly accepted approach is using nonlinear springs instead of linear ones within the energy harvester.

One successful physical realization of nonlinear spring is the hardening mechanism approach. An example of a MEMS energy harvester with a hardening mechanism can be seen in Figure 1.4.
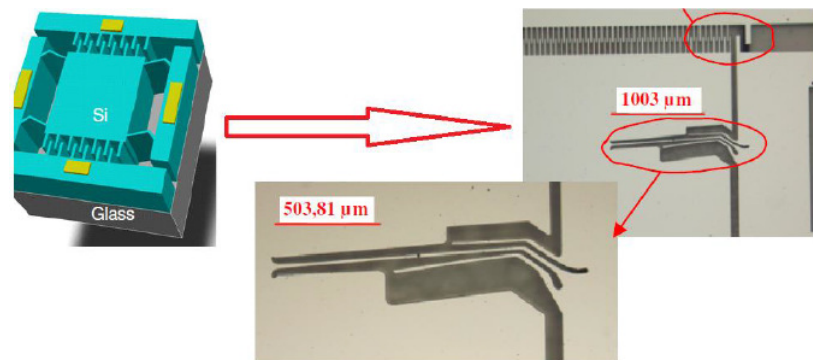
Figure 1.4. Example of hardening mechanism [7]

The idea of the hardening mechanism can be summarized as designing the spring of the proof mass such that the spring constant, k, increases as the proof mass approaches to the boundaries of its travel span [7]. In other words, the spring constant of the system is intended to be maximum when the proof mass is at its boundary limits and minimum as its passing through midpoint of the travel distance. By this way, the average velocity of the proof mass is tried to be increased and also collusion with boundaries is tried to be prevented.

However, further studies showed that although using these springs may increase the efficiency up to 27 % compared with linear springs [8], this approach does not solve the problem of variable frequency range of environment problem. They still require proper and

slow frequency sweep from the environment in order to keep the efficiency in high levels [9].

Another well know approach is bistable mechanism offering. An illustrative sketch of this idea can be seen in Figure 1.5.
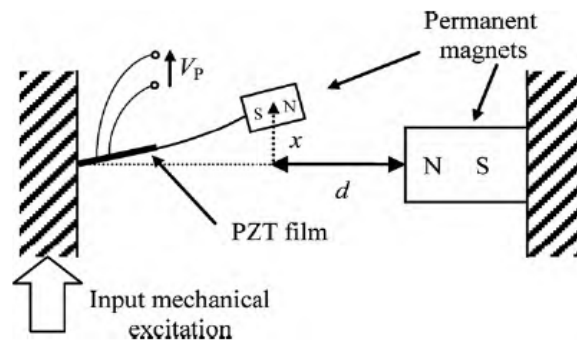
Figure 1.5. Example of bistable mechanism [9]

Bistable mechanisms use the idea of creating nonlinearity by adding an external force to the system that acts on the proof mass and makes it hard to maintain the position at the midpoint of the travel span. By this way, the average velocity of the proof mass is planned to be increased just like the hardening mechanism.

However, again further researches showed some drawbacks of these mechanisms. They require either a large amplitude periodic force or low amplitude periodic force with perturbation. If the amplitude of the ambient vibration level is not above a certain threshold value, the proof mass cannot move from one state to another. In that case, a limited amount of power can be harvested from it. It oscillates around a equilibrium position with a locally linear behaviour [9].

In addition to all of these drawbacks, in general for all nonlinear spring approaches it can be said that they are all hard to fabricate with current MEMS production techniques [7] and they do not provide better performance when the ambient vibration source is random [10].

The piezoelectric multifrequency generators can be considered as another approach for solving efficiency problems of energy harvesters. In that approach, the main idea is placing several piezoelectric beams with different spring constants inside of a harvester (see Figure

1.6)[11]. Since each beam has different resonant frequency values, it is aimed to increase the frequency range that the harvester works efficiently.
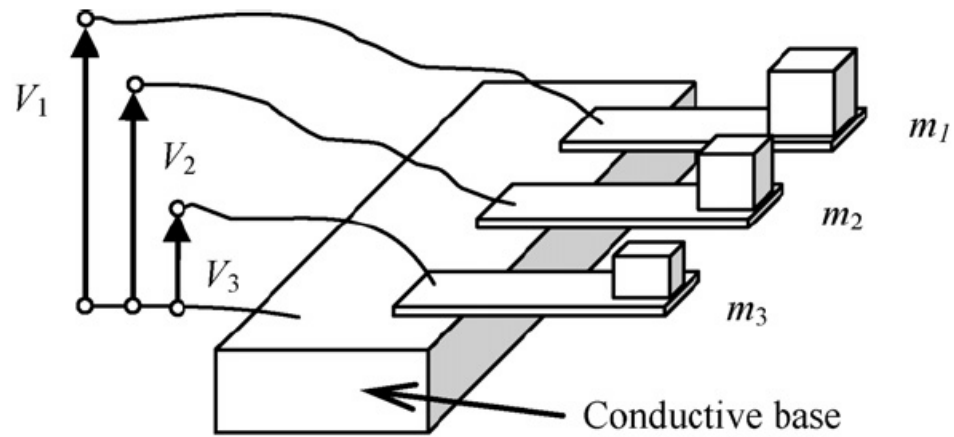
Figure 1.6. Piezoelectric multifrequency generator [11]

However, since some of the piezo beams vibrates at their resonant frequency value while the rest of them vibrates poorly at a given ambient vibration frequency, the overall efficiency of the system does not increase too much comparing with conventional energy harvesters. What is more, the problem of limited travel span is not solved. The PM of the system still can collide with the boundaries and cause efficiency decrease under variable ambient vibration conditions.

2. PROPOSITION: NONLINEAR DAMPING

The problems and some of the design alternatives associated with designing a better performance energy harvester are mentioned in the previous sections. As seen, the proposed solutions are concentrated on replacing linear springs with nonlinear ones for increasing the optimal working range under variable vibration frequency and amplitude conditions. As an alternative approach, our suggestion and the subject of this thesis is using a nonlinear damping mechanism instead of a linear one to solve the mentioned problems and increase the harvester's efficiency. This chapter of the thesis is mainly focused on describing the nonlinear damping mechanism for a vibration based energy harvester and theoretical modelling.

2.1. DESCRIPTION

In conventional electromagnetic energy harvesters, there is a damping force caused by the magnetic field acting on the moving proof mass. This damping is called the electrical damping as electricity is generated as a result of this damping. Moreover, this damping force is linear i.e. the damping is constant along the travel span. (See Figure 2.1.(a)).
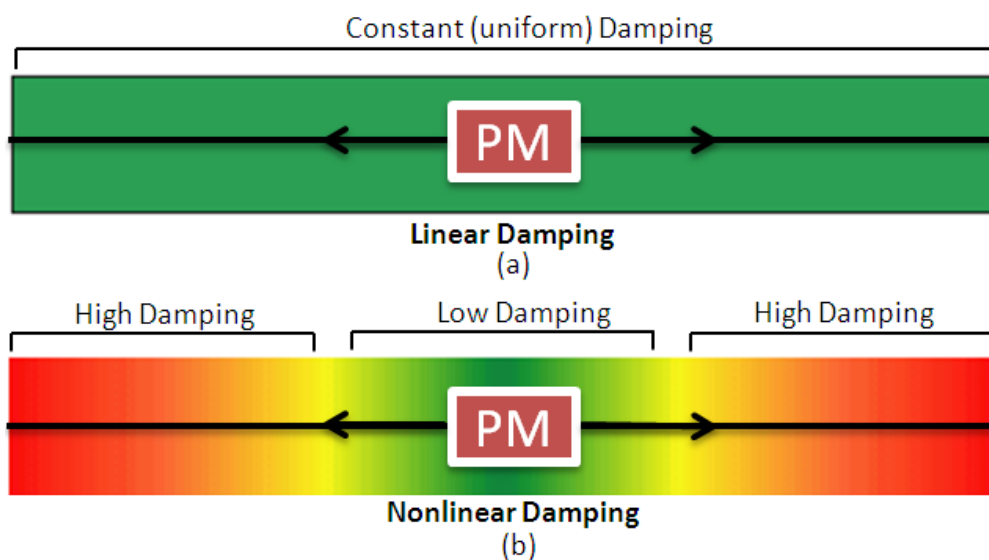
Figure 2.1.   Damping distributions along travel span: **(a)** linear damping **(b)** nonlinear damping

In our approach, it is suggested to create higher damping at the boundaries and lower damping at the midpoint of the PM's travel span. By this way, the PM will face maximum resistance as it approaches to the boundaries, which will also prevent collusion. On the contrary it will experience minimum resistance as it passes through midpoint of its travel span. With this nonlinear damping profile, it is aimed to increase the ambient vibration frequency and amplitude range that the device works with high efficiency performance.

2.2. THEORY AND MODELLING

Theoretical model is the first step of analysis of the feasibility of nonlinear damping proposal. In order to model the system accurately, we first begin with the basic model of a vibration energy harvester. After that, nonlinear damping terms are added to the model. At the end of the theoretical modelling, appropriate equations are used to calculate the harvested electrical power under given ambient vibration. This section of the thesis report describes all these in detail.

2.2.1. Equation of Motion of a Vibration Energy Harvester

A vibration energy harvester is conventionally modelled as a spring-mass-damper system. An illustrative sketch of this model can be seen in Figure 2.2.
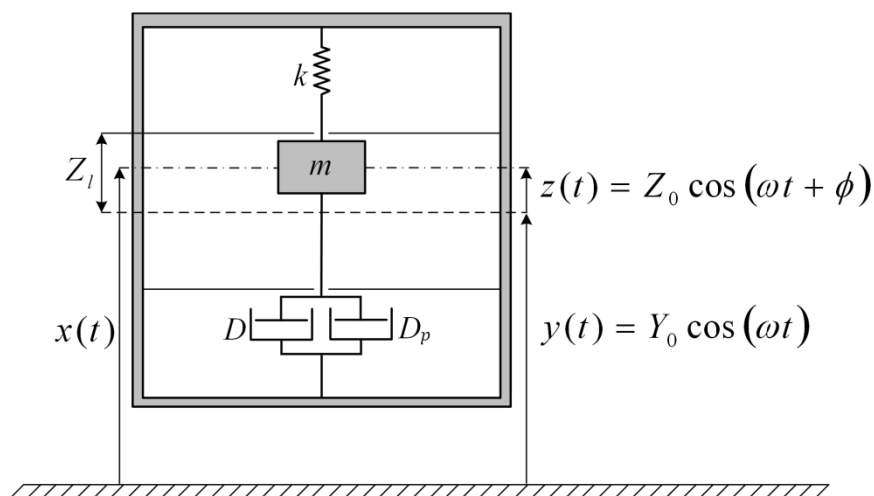
Figure 2.2. Model of a vibration driven system

In this model, the amount of frame displacement caused by the ambient vibration is represented by y(t) term. z(t) term represents the relative displacement of the PM with respect to the frame. The representative term of absolute displacement of the PM, x(t), is therefore equal to the sum of y(t) and z(t). To be able to create a more realistic model, the travel range of the PM is constrained by the boundaries. In this model Z_l shows the location of the boundary in positive direction. Therefore the allowed travel distance of the PM is between the locations of $z(t) = -Z_l$ and $z(t) = Z_l$. These constraints will play important role in power calculations.

After all these parameters are defined, the equation of motion of the PM can be written as follows:

$$m\ddot{z}(t) + kz(t) + D\dot{z}(t) + D_p\dot{z}(t) = -m\ddot{y}(t) \tag{2.1}$$

In Equation 2.1, "m" term represents the mass of the PM in unit of kg. "k" term represents the spring constant of the device which is assumed to be linear in our study. The damping is represented with two different terms in the equation D and D_p. D_p is the parasitic damping constant, which can be considered as loss of energy due to frictional loses etc. D is the electrical damping constant caused by the electromagnetic induction within the device. It should be noted that the frame displacement y(t) is considered to be unaffected by the harvester in this study. The motion of the frame and the PM are assumed to be harmonic. Therefore the following equalities can be written:

$$y(t) = Y_0\cos(\omega t) \tag{2.2}$$

$$\dot{y}(t) = -\omega Y_0\sin(\omega t) \tag{2.3}$$

$$\ddot{y}(t) = -\omega^2 Y_0\cos(\omega t) \tag{2.4}$$

$$z(t) = Z_0\cos(\omega t + \varphi) \tag{2.5}$$

$$\dot{z}(t) = -\omega Z_0\sin(\omega t + \varphi) \tag{2.6}$$

$$\ddot{z}(t) = -\omega^2 Z_0 \cos(\omega t + \varphi) \tag{2.7}$$

where Y_0 and Z_0 being the amplitude of frame motion and PM motion, respectively, and ω being the frequency of the ambient vibration.

2.2.2. Introducing Nonlinear Damping

In Equation 2.1, the model is created with linear damping, D. In order to model the nonlinear damping, the linear damping term $(D\dot{z}(t))$ is replaced by nonlinear term $(D_n|z|^n \dot{z}(t))$ and the equation of motion becomes

$$m\ddot{z}(t) + kz(t) + D_n|z|^n \dot{z}(t) + D_p \dot{z}(t) = -m\ddot{y}(t) \tag{2.8}$$

In Equation 2.8, the degree of nonlinearity term n is introduced. It can be seen that in this equation, the electrical damping is directly related to the absolute value of nth power of the relative PM displacement. As the degree of nonlinearity, n, increases, the electrical damping profile changes accordingly.
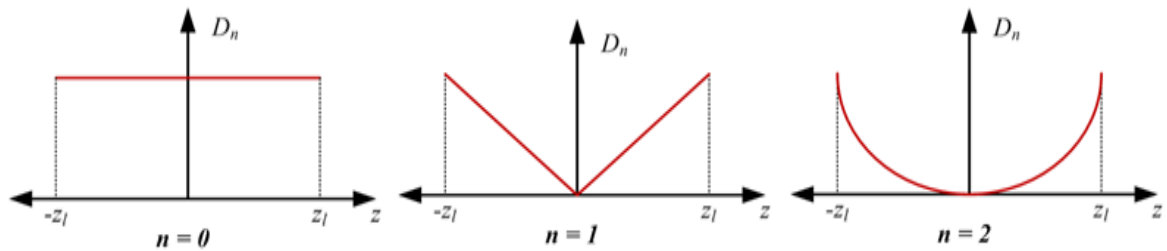
Figure 2.3. The effect of n on electrical damping profile

The effect of n can be clearly seen in Figure 2.3 for three different cases. While $n = 0$, the equation behaves like a linear damping case. The damping does not change along the travel span of the PM. When $n = 1$, the damping increases linearly as the PM approaches to its upper and lower boundaries. Also when $n = 2$, damping changes parabolically. This model allows us to apply different types of nonlinearity profiles and see their effects on the harvester efficiency.

Since the harmonic motion assumption was made before, $\ddot{y}(t)$ term of Equation 2.8 can be replaced with Equation 2.4. After this replacement, the final version of the equation of motion can be expressed as follows:

$$m\ddot{z}(t) + kz(t) + D_n|z|^n\dot{z}(t) + D_p\dot{z}(t) = m(\omega^2 Y_0 \cos\omega t) \tag{2.9}$$

2.2.3. Power and Efficiency

As mentioned before, the motion of the PM in a real energy harvester is limited by boundaries. Therefore, to be able to create a realistic equation for harvested power, this restriction should be considered. The equation to calculate the maximum power that can be extracted from a harvester with a linear damping mechanism has been previously derived [12] as:

$$P_{linear} = \frac{2D}{T}\int_{z=-Z_l}^{Z_l} \dot{z}\,dz = \frac{2D}{T}\int_0^{T/2} \dot{z}^2\,dt \tag{2.10}$$

where T represents the vibration period $(2\pi/\omega)$. This equation represents the amount of power that can be extracted over one period of PM motion. If we go further and solve the Equation 2.10, first, we have to construct the relationship between Y_0 and Z_0 by substituting the damping ratio, $\zeta = D/2m\omega_n$, resonant frequency, $\omega_n = \sqrt{k/m}$, and the harmonic balance assumption equations (Equation 2.2-Equation 2.7) into Equation 2.1 and take the Laplace transform, which leads:

$$\frac{Z(s)}{Y(s)} = \frac{-s^2}{s^2 + 2\zeta\omega_n s + \omega_n^2} \tag{2.11}$$

After that, Equation 2.11 can be converted into time domain as follows:

$$\frac{Z_0}{Y_0} = \frac{\omega_c^2}{\sqrt{(1-\omega_c^2)^2 + (2\zeta\omega_c)^2}} \tag{2.12}$$

where $\omega_c = (\omega/\omega_n)$. Finally, solving the integral in Equation 2.10 with the Z_0 got from Equation 2.12 and multiplying the result by frequency gives energy harvested in one period (i.e. power) [12]:

$$P = \frac{\zeta \omega_c{}^3 Y_0{}^2 \omega^3 m}{[1 - \omega_c{}^2]^2 + [2\zeta\omega_c]^2} \tag{2.13}$$

The approach used for calculating power for the linear case can be applied to the nonlinear damping case. Therefore $(D\dot{z})$ of the Equation 2.10 is replaced with $(D|z|^n\dot{z})$ term. The resulting equation can be seen in Equation 2.14.

$$P_{\text{nonlinear}} = \frac{2D_n}{T} \int_{z=-Z_l}^{Z_l} \dot{z}|z|^n dz \tag{2.14}$$

Since Equation 2.14 is highly nonlinear, coming up with an analytical solution for it as in Equation 2.10 is not an easy task. Therefore, numerical methods are used, as they will be explained in Chapter 3.

Finally, in order to obtain a measure of energy harvester's efficiency, the power results obtained from Equation 2.10 and Equation 2.14 should be nondimensionalized as shown below:

$$P^* = \frac{P}{Y_0{}^2 \omega^3 m} \tag{2.15}$$

It should be noted that all power results presented in this thesis report are nondimensional values.

3. COMPUTATIONAL STUDY

In the previous chapters, the nonlinear damping concept is described and modelled in detail. In this chapter, the efficiencies of linear and nonlinear dampings are compared by solving the equations of power (Equation 2.10 and Equation 2.14) numerically for a range of base excitation amplitudes and frequencies. This way, the nonlinear damping concept is numerically validated in different conditions.

3.1. GENERAL DESCRIPTION OF SIMULATIONS

The simulation results are obtained by solving Equation 2.8 and Equation 2.14 consecutively. If we look at these equations, it can be seen that solving them analytically for nonlinear cases is a very complicated task. For this reason, it is decided to use numerical approaches for the analysis. The built-in function called ODE45 of MATLAB is used to solve the differential equations of motion for $z(t)$ numerically. Once $z(t)$ is found, the power is calculated by evaluating Equation 2.14 numerically again in MATLAB.

To compare the efficiencies of nonlinearly damped systems with linear ones, it is decided to go with two different nonlinearity profiles. Therefore, to simulate nonlinear damping, the nonlinearity term, n, appearing in Equation 2.9 and Equation 2.14 is selected as $n = 1$ and $n = 2$. The physical meanings of these nonlinearity values were described before and can be seen in Section 2.2.2. Also to be able to compare them with conventional linearly damped systems, $n = 0$ case is also included in the simulations. For all these three different profiles, two different parasitic damping scenarios are used. In the first scenario, parasitic damping of the system is set to zero to see the effect of nonlinearity under ideal conditions. In other words, it is assumed that there is no loss in the system due to friction, etc. For the second scenario, three different amount of parasitic damping is added to the simulations to see the effect of parasitic damping on the performance i.e. efficiency of the system and to get more realistic results.

For each scenario, the nondimensional power outputs of all selected damping profiles are calculated over a specified $\omega^* = \omega/\omega_n$ and $z^* = Z_l/Y_0$ range. At the end of each

simulation, for example, for "a" ω^* values and "b" z^* values, resultant power is obtained in the form of (axb) matrix. At the end, the script is being able to test whole testing range with a given specific increments. All other parameters besides ω^* and z^* are kept constant for the sake of consistency. These constant parameters can be seen in Table 3.1. After calculating all individual power values for related base excitation amplitudes and frequencies, the results are non-dimensionalized as seen in Equation 2.12.

Table 3.1. Simulation parameters

Parameter	Value
m [kg]	0.02
ω^*	0.1 – 2.0
z^*	0.1 – 1.0
k [N/m]	120
Z_l [m]	0.01

It should be noted that, at each power calculation, it is assumed that the damping constant, D_n, of the system is calculated adaptively in order to get maximum efficiency. In order to achieve this, a subroutine called "Damping Constant Optimization Subfunction (DCOS)" is coded. The flowchart of the algorithm for determining optimum D_n that results in extracting maximum power for each data set pair is explained in Figure 3.1. This subfunction will be used within the main simulation algorithm later.
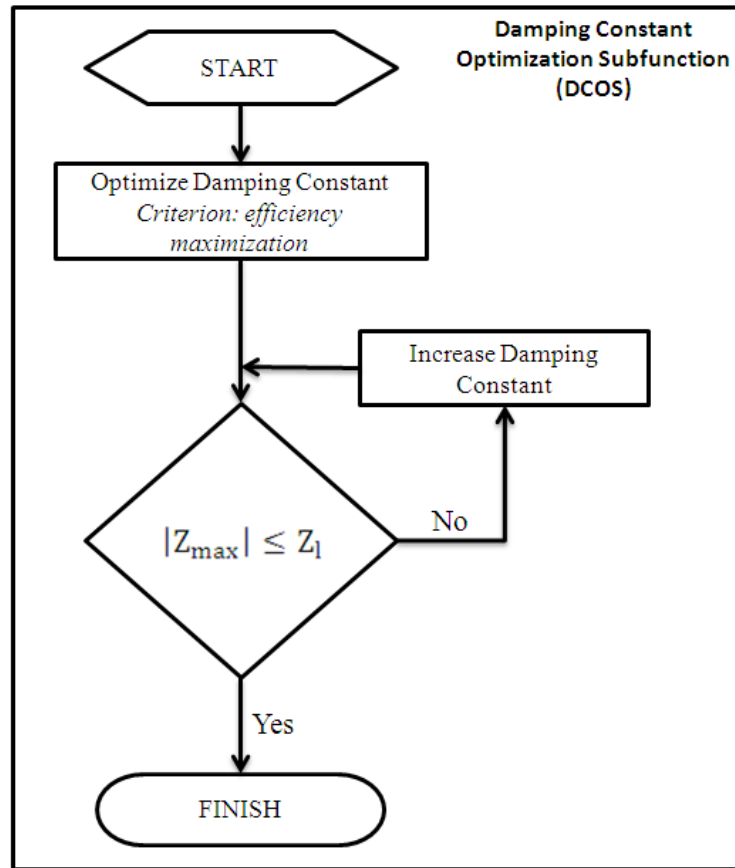
Figure 3.1. D_n Optimization flowchart

The DCOS algorithm first calculates the optimizing D_n value required for the given ω^* and z^* input to get the maximum power output. The MATLAB command used for this task is "fminsearch" which is included in the Optimization Toolbox. After D_n converges, the algorithm calculates the motion profile of the PM and checks if any collusion occurs between the PM and the boundaries. If there is collusion, the damping constant, D_n, is increased until no collusion occurs. The reason for doing that is to prevent losses caused by collusion and to prevent calculation errors, since any loss from collision is not modelled. After finding the appropriate damping value, DCOS delivers this value to the main code. The rest of the calculations are handled in the main code.
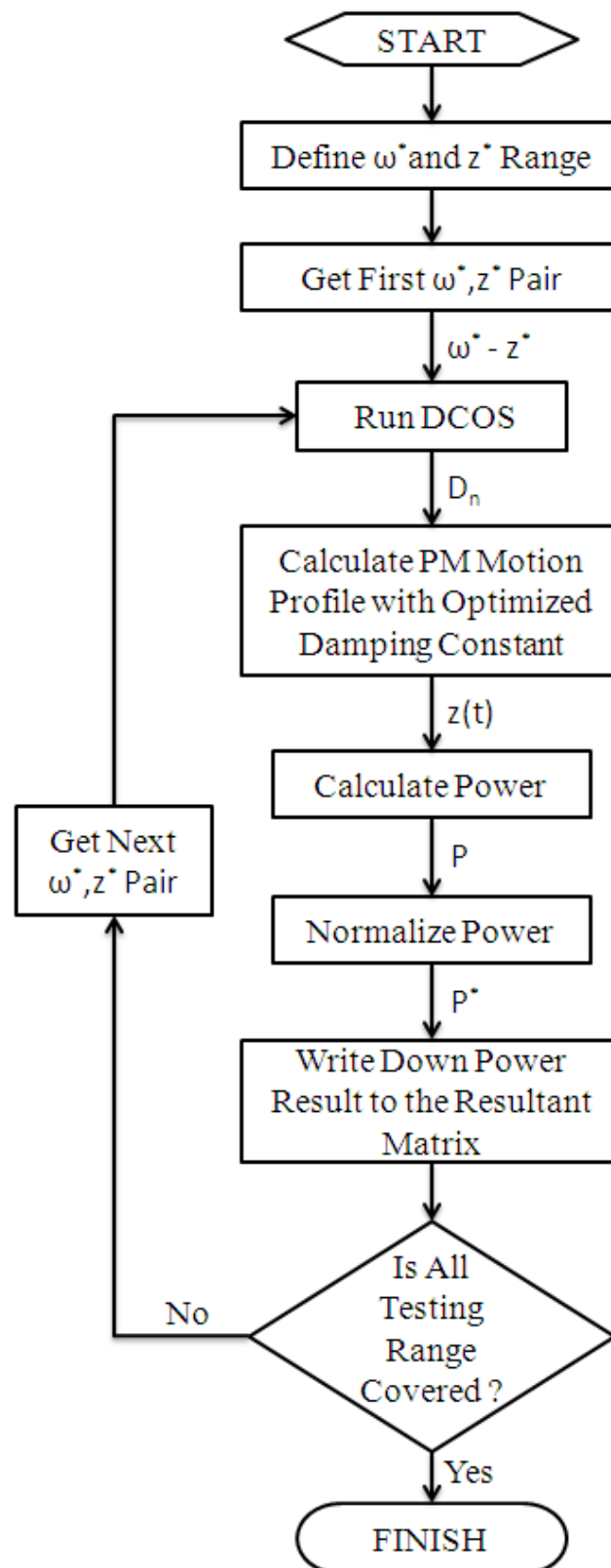
Figure 3.2. General flowchart of the main code

The overall flow chart of the simulations can be seen in Figure 3.2. After the initialization i.e. defining the test range by providing the ω^* and z^* pairs, the script first gets the ω^* and z^* values. With the current ω^* and z^* values DCOS script is run to calculate the damping constant D_n that optimizes power. After D_n is calculated, the main code calculates the motion profile of the PM by solving Equation 2.8 numerically for the time period of $[0, \frac{16\pi}{\omega}]$. After that, by using the calculated motion profile, it calculates the power by numerically solving Equation 2.14, nondimensionalizes the power using Equation 2.15, stores the nondimensionalized power result and re-runs DOCS with the next ω^*, z^* pair. This loop continues until the whole ω^*- z^* range is covered.

It should be noted that for the physical realization perspective of this scenario, it is assumed that ω^* and z^* values can be measured during operation and all these measurement and calculation processes to consume no power. The codes used in these simulations are given and can be seen in Appendix Table A1.

3.2.   SIMULATION RESULTS

After calculating the nondimensionalized powers for all three damping profiles and two different scenarios, the results are plotted and shown on three dimensional graphs. Here, firstly the power output results of linear $n = 0$ profile and also nonlinear $n = 1$ and $n = 2$ profiles are demonstrated individually. These results are obtained for zero parasitic damping case ($D_p = 0$).
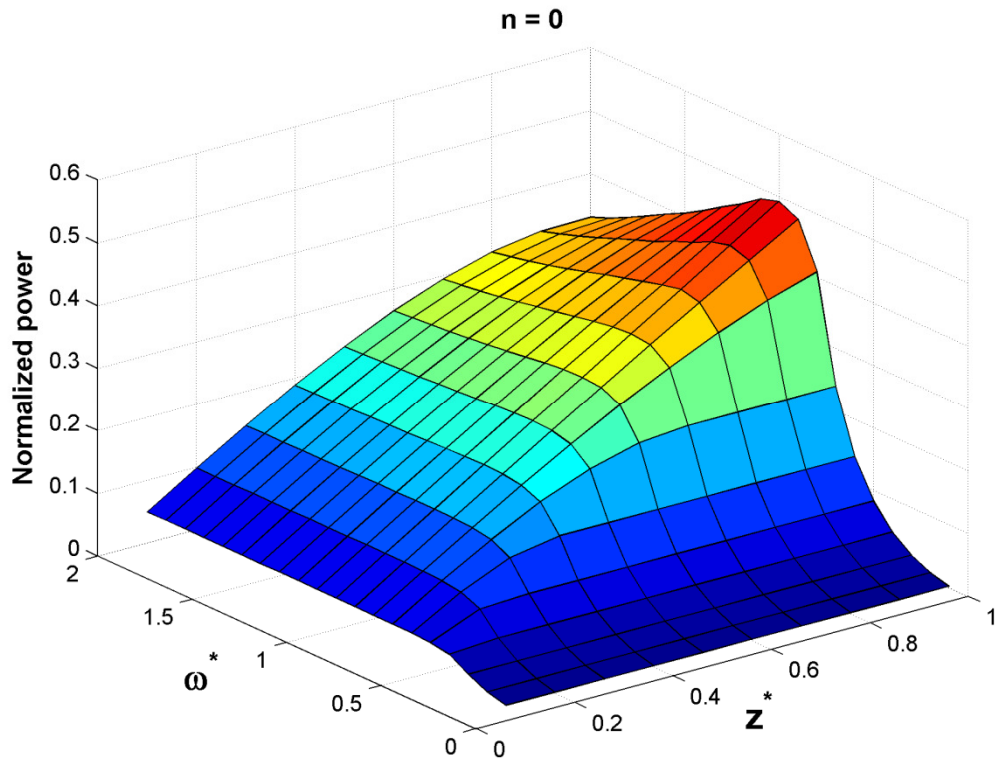
Figure 3.3. Simulation result of $n = 0$ profile ($D_p = 0$)

Figure 3.3 shows the simulation results of $n = 0$ linear damping profile under ideal circumstances ($D_p = 0$). At the first look, it can be concluded that the result appears as it is predicted before. The maximum power that can be extracted is highest on the resonant value line where $\omega^* = 1$. The figure indicates that the average harvested power increases as z^* value approaches to 1 in general. Also the system loses efficiency dramatically below the value of 0.5 for ω^*.
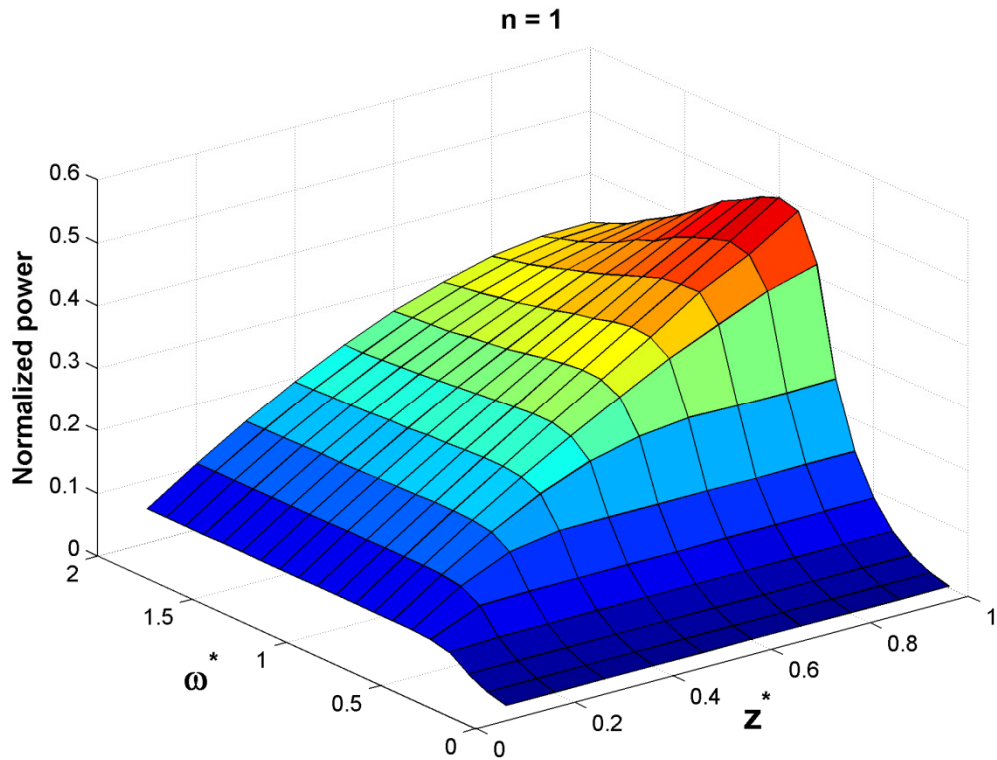
Figure 3.4. Simulation result of $n = 1$ profile ($D_p = 0$)

Figure 3.4 and Figure 3.5 shows the results of nonlinear damping cases respectively. It is seen that when we look overall, the linear and nonlinear system power results seem to have the same pattern over the given base excitation data set range. Although it is hard to compare their efficiencies from these graphs, it can be concluded that some slight changes occur as the degree of nonlinearity increases. The comparison of them will be done in the next section.
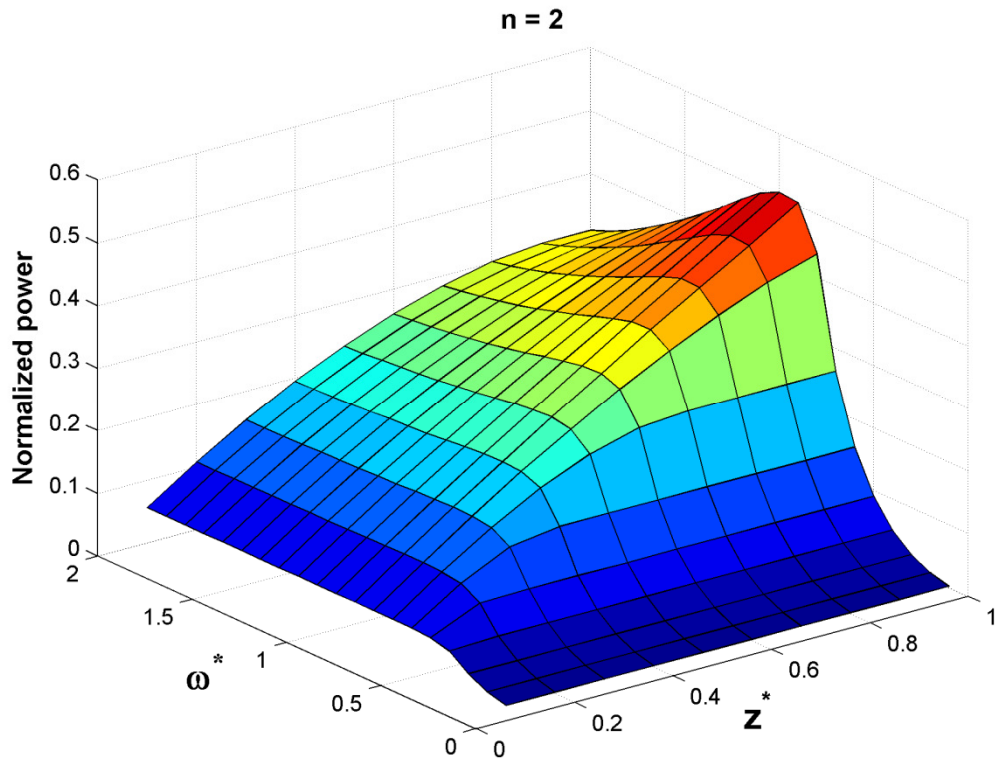
Figure 3.5. Simulation result of $n = 2$ profile $(D_p = 0)$

3.2.1. Efficiency Without Parasitic Damping

As it was mentioned before, the simulations are run first with no parasitic damping case to see the effects of nonlinearity under ideal conditions. Under those circumstances, linear $(n = 0)$ and nonlinear $(n = 1, n = 2)$ profiles are simulated individually. This section of the report intends to compare the two nonlinear damping profiles with the linear one.

Figure 3.6 compares the efficiencies of $n = 1$ and $n = 2$ with respect to $n = 0$. Figure 3.6.(a) shows the efficiency difference between $n = 1$ and $n = 0$ and Figure 3.6.(b) shows the efficiency difference between $n = 2$ and $n = 0$ damping profiles individually. In both figures the x axes indicates the z^* values while y axes indicates the ω^* values respectively. Contour values shows the difference between efficiencies i.e. $P^*(n = 1) - P^*(n = 0)$ for Figure 3.6.(a) and $P^*(n = 1) - P^*(n = 0)$ for Figure 3.6.(b).

As seen from the figures, the nonlinear damping cases resulted in higher efficiency compared with the linear case in the majority of the areas within the test range, meaning that nonlinear damping gives better results in these regions. For both $n = 1$ and $n = 2$ damping profiles, it can be concluded that the efficiency increase compared to linear model is mainly within $0.4 < \omega^* < 1.5$ range. The efficiency increase is maximum slightly below the resonance ($\omega^* = 1$) for both cases. The maximum efficiency increase for the first order ($n = 1$) system is measured as 0.015 whereas the maximum efficiency increase for the second order ($n = 2$) system is measured as 0.029. Using this result, we can conclude that the efficiency increase within the range where nonlinear profiles give better results is directly related to the degree of nonlinearity; i.e. as the degree of nonlinearity increases, the efficiency increment increases. However, for both profiles, the efficiencies of linear and nonlinear models seem to be more or less the same below the line of $\omega^* \leq 0.3$. What is more, from the acquired results it is seen that for both cases the linearly damped model gives better results than the nonlinear ones where $\omega^* > 1.4$ and $z^* > 0.5$. The reason of this situation can be explained as the level of excitation amplitude and frequency does not allow PM to travel all through its travel span and remains mostly in the middle. In other words, the PM remains within the low damping region of nonlinear damping system and the extracted power decreases as a result.

(a)   (b)
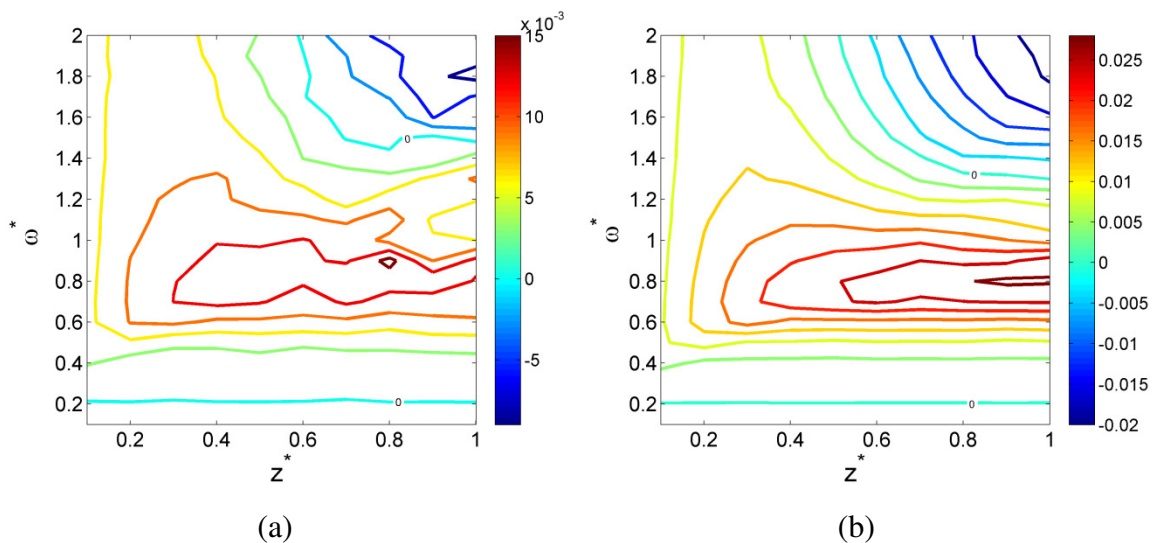
Figure 3.6.   Comparison of efficiencies of the without parasitic damping scenario: **(a)** difference between $n = 1$ and $n = 0$ **(b)** difference between $n = 2$ and $n = 0$

Figure 3.7. reveals the percentage efficiency change for both nonlinear profiles compared to linear one. These two graphs are plotted to have a clear opinion about the effects of nonlinearities. Again in these graphs x axes indicates the z^* values while y axes indicates the ω^* values respectively.

In Figure 3.7.(a) the percent difference of the first order system compared to a linear system is shown. The method used to calculate this result is to simply calculate percentage deviation of $n = 1$ case results from $n = 0$ results; i.e. $((P^*(n = 1) - P^*(n = 0)) / P^*(n = 0)) \times 100$. It can be observed that within the range of $z^* < 0.2$ and $0.4 < \omega^* < 0.9$ region the proposed first order nonlinear system is superior to linear system up to 10 % increase in efficiency. Although the nonlinear system is more efficient in most of the regions, there is a relatively small region located on $z^* > 0.6$ and $\omega^* > 1.4$ area where conventional system look superior but this superiority is just going up to 2 % which can be considered as relatively small compared to gains of nonlinear system.

(a)   (b)
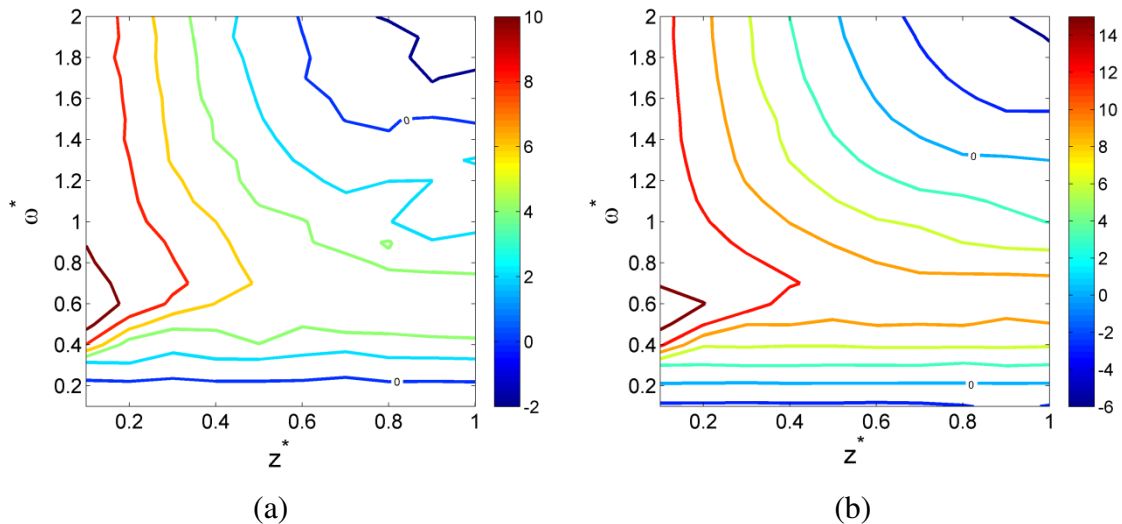
Figure 3.7. Percent difference results of without parasitic damping scenario: **(a)** percentage difference between $n = 1$ and $n = 0$ **(b)** percentage difference between $n = 2$ and $n = 0$

Figure 3.7.(b) shows the efficiency percentage comparison of second order nonlinear system compared to linear system. The same calculation method for calculating percent difference is applied here also i.e. $((P^*(n = 2) - P^*(n = 0)) / P^*(n = 0)) \times 100$. It can be said that the graph is more or less the same with Figure 3.7.(a). The second order system is also better than linear system in most of the regions. The most effective region

seems to be located between $z^* < 0.3$ and $0.4 < \omega^* < 0.7$. The important result that can be concluded from this graph is that the percent change in efficiency by the second order nonlinear system goes up to 15 %, which is a greater value than the maximum efficiency increase that can be get from the first order nonlinear system. Just like the first order comparison, there is again a region where second order system gives poorer results but this time the superiority of the linear system goes up to 6 %.
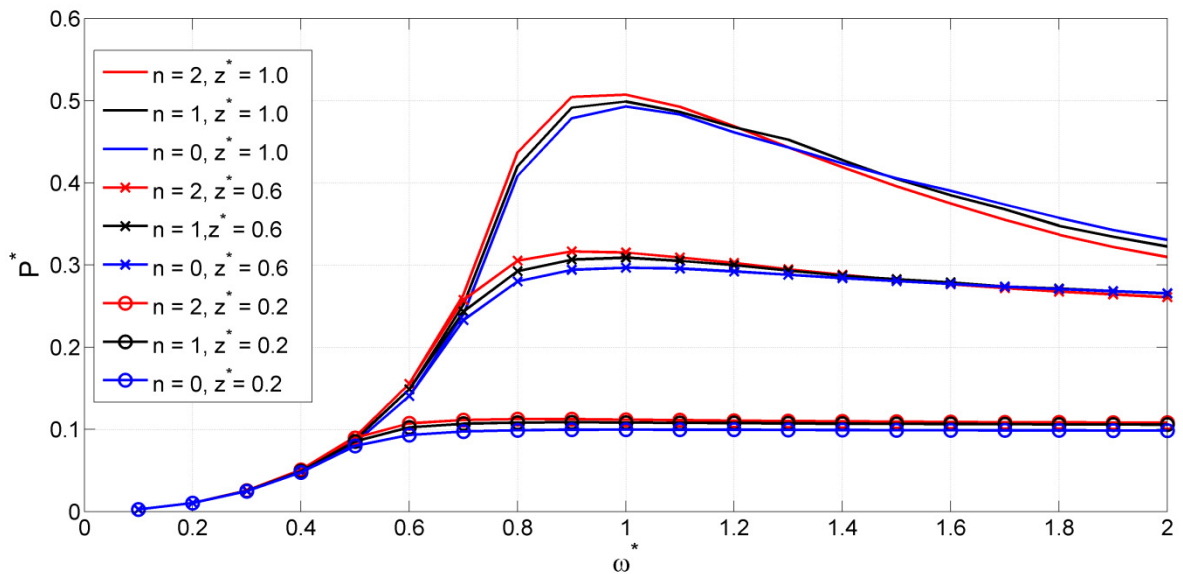
Figure 3.8. P^* comparison for different level of excitation amplitudes

To see the effect of z^* on the performance of different models clearly, Figure 3.8 is plotted. In that figure x axis shows the ω^* value while y axis indicates the nondimensionalized power results. There can be seen three separate groups of lines on the graph. These groups represent the nondimensionalized power results of systems subjected to different base excitation amplitudes. From that figure, at the first sight, it can be said that the efficiency of all three models increases as the base excitation amplitude increases as expected. When z^* value equals to 0.2, it can be seen that as the nonlinearity of the system increases, the efficiency of the systems increases no matter what value does ω^* ratio takes. If we look at the group of lines plotted for $z^* = 0.6$ ratio it is seen that the degree of nonlinearity is important up to the value of 1.5 for ω^* ratio. If we go further and increase the z^* ratio up to 1.0, it is clear that the nonlinear systems give better performance just up to $\omega^* = 1.2$.

3.2.2. Efficiency With Parasitic Damping

In a real physical energy harvester, it is obvious that there will be some amount of parasitic damping. Because of that phenomenon, in the second part of the simulation study, some amount of parasitic damping is added to the model. For that purpose, it is decided to use three different levels of parasitic dampings. The selected damping ratios can be listed as $\zeta_p = 0.01$, $\zeta_p = 0.1$ and $\zeta_p = 0.5$. The reason for choosing to work with different levels of parasitic dampings is to have full idea on the effect of parasitic damping on the efficiencies of the proposed systems. The same method followed on the previous scenario is applied again for this scenario. The plots presented in this section show the percent efficiency differences of the nonlinear systems compared with linear ones.

(a)   (b)

Figure 3.9.   Percent difference between efficiencies with $\zeta_p = 0.01$ parasitic damping ratio: percent difference of **(a)** $n = 1$ and **(b)** $n = 2$, with respect to $n = 0$.

Figure 3.9 shows the results of the percent efficiency differences of the proposed models with the linear model.

Figure 3.9.(a) reveals the percentage difference between efficiencies of first order nonlinear system with the linear system while the model is subjected to parasitic damping with the damping ratio of $\zeta_p = 0.01$. If we compare the percent efficiency difference for $\zeta_p = 0$ case presented in Figure 3.7.(a) with this result, it is seen that the regions where first order nonlinear system is superior start to shrink. The parasitic damping reduces the efficiency increase of the proposed system.

Figure 3.9.(b) shows the percentage difference between the efficiencies of second order nonlinear system with linear system again while the system is under the effect of parasitic damping with $\zeta_p = 0.01$. The same comments made for Figure 3.9.(a) can be made for this plot as well. The regions where $n = 2$ is better get narrower.

<div align="center">(a)   (b)</div>
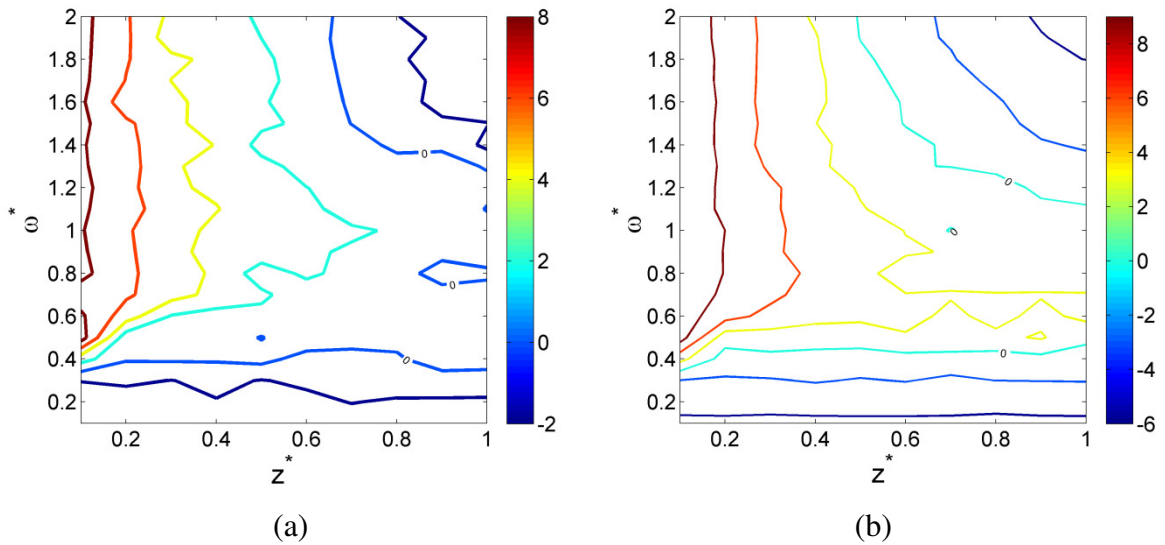
Figure 3.10.   Percent difference between efficiencies with $\zeta_p = 0.1$ parasitic damping ratio: percent difference of **(a)** $n = 1$ and **(b)** $n = 2$, with respect to $n = 0$.

If we increase the parasitic damping a little more, the results shown in Figure 3.10 are obtained. Figure 3.10.(a) shows the percent difference between efficiencies of first order nonlinear system over linear system while Figure 3.10.(b) shows the percent difference between efficiencies of second order nonlinear system over linear system under the effect of parasitic damping with the damping ratio of $\zeta_p = 0.1$. When we compare these results with the previous ones, it is seen that the regions where nonlinear systems are more efficient shrink further. Also if we compare the maximum efficiency increments of the proposed systems get for $\zeta_p = 0.01$ damping ratio with the $\zeta_p = 0.1$ damping ratio case, it is seen that for $n = 1$, the maximum efficiency increase gets down from 10 % to 8 % and for $n = 2$, it gets down from 12 % to around 9 %.

When we increase the parasitic damping ratio to $\zeta_p = 0.5$, the results shown in Figure 3.11 are obtained. The Figure 3.11.(a) shows the percent difference between efficiencies of first order nonlinear system over linear system and Figure 3.11.(b) shows the percent different efficiencies of second order nonlinear system over linear system under the effect of

parasitic damping ratio of $\zeta_p = 0.5$. The results for both proposed systems indicate that for that level of parasitic damping we do not see any more performance improvements over linear system for the majority of the testing range.
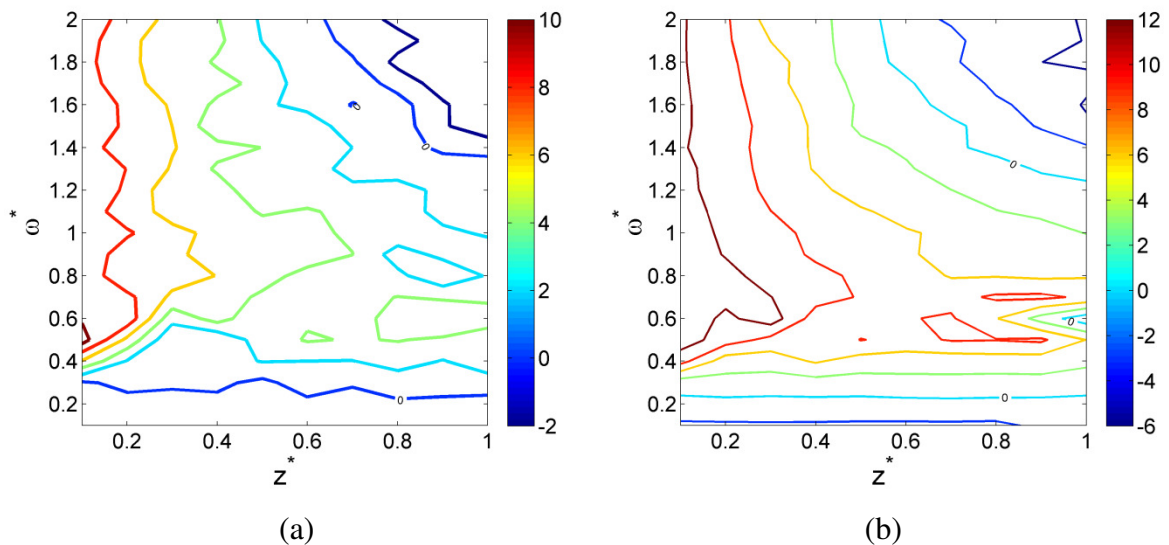

| (a) | (b) |
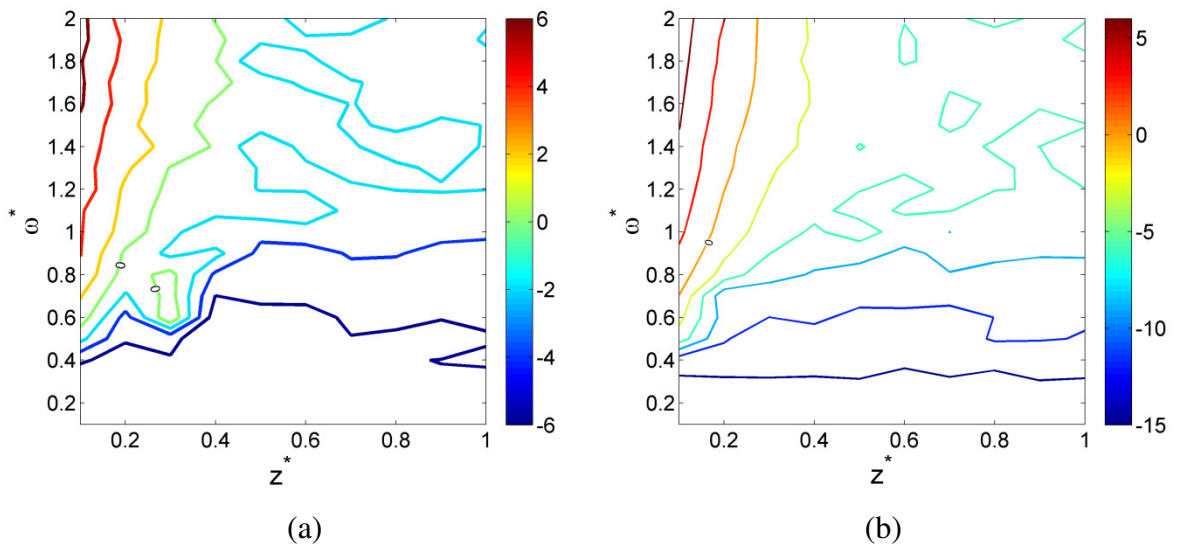
Figure 3.11. Percent difference between efficiencies with $\zeta_p = 0.5$ parasitic damping ratio: percent difference of **(a)** $n = 1$ and **(b)** $n = 2$, with respect to $n = 0$.

These three simulations show us that parasitic damping of the energy harvester has a direct effect on the proposed systems' performance. As the level of parasitic damping increases, the performance increase of nonlinear damping decreases. In other words, the efficiency gain of nonlinear damping gets lost. The possible reason of this phenomenon is discussed in section 3.5.

3.3. CONVERGENCE ANALYSIS

Since the power calculations are done numerically, the convergence of ODE45, function of MATLAB should be checked with different parameters. The relative vibration $z(t)$ should be a periodical signal with fixed amplitude in steady state. In order to check that, for randomly selected base excitation frequency and amplitude values, the steady state of the relative PM motion, $z(t)$ plots are observed. In Figure 3.12, the $(z(t))$ plots for linear and first order nonlinear systems are shown for $\zeta_p = 0$ scenario. Also in Figure 3.13 the $z(t)$ plots for linear and first order nonlinear systems are shown for $\zeta_p = 0.1$ scenario, All plots

include zero initial condition and non-zero initial condition cases individually. The other selected parameters for these plots can be seen in Table 3.2.

(a)   (b)
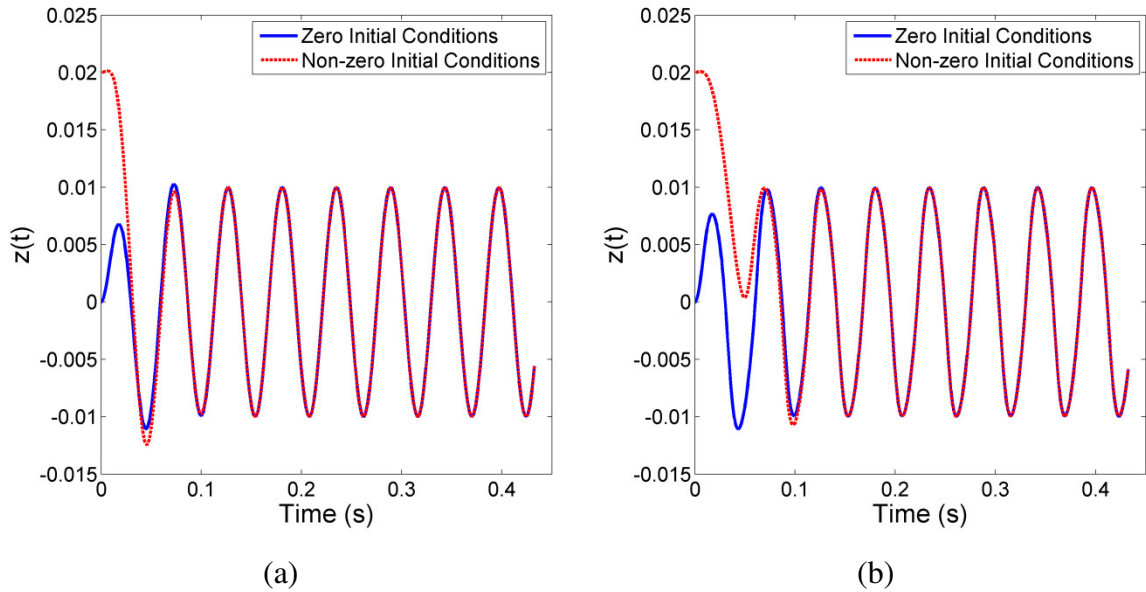
Figure 3.12.   Example $z(t)$ plots for convergence check, $\zeta_p = 0$ **(a)** $n = 0$ case **(b)** $n = 1$ case

(a)   (b)
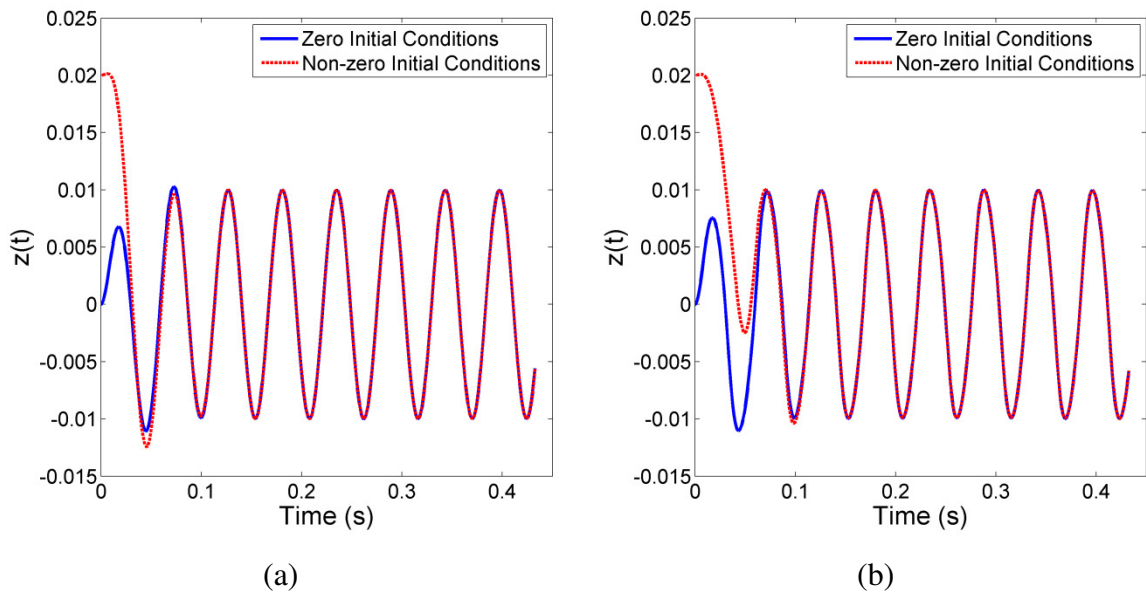
Figure 3.13.   Example $z(t)$ plots for convergence check, $\zeta_p = 0.1$ **(a)** $n = 0$ case **(b)** $n = 1$ case

Although the time range provided to the ODE45 for real simulations is $[0, 32\pi/\omega]$ which provides us sixteen period of motion, the results demonstrated in Figure 3.12 and Figure 3.13 are plotted with $[0, 16\pi/\omega]$ time range for visual purposes. If we look at Figure

3.12.(a) and Figure 3.12(b) individually it can be concluded for both of them that the results of ODE45 solver seems to be converges for both zero and non-zero initial condition cases respectively. The same conclusion can be made for parasitic scenario figures of Figure 3.13.(a) and Figure 3.13.(b) as well.

Even if there seems to be a transient part at each case, it should be noted that these transient parts of the solutions are omitted by the script and not added to the power calculations. Since the only effect of non-zero initial condition cases seem to be on these transient parts, we can also say that this case does not affect the results as well.

As a result it can be said that these transient parts and initial conditions have no disturbance effects on the simulation results. All in all, one can conclude that the simulation results presented in this report can be counted as accurate in terms of convergence performance of the MATLAB's ODE45 solver.

Table 3.2. Selected parameters for convergence tests

	Figure 3.12.(a)	**Figure 3.12.(b)**	**Figure 3.13.(a)**	**Figure 3.13.(b)**
Parameter	**Value**	**Value**	**Value**	**Value**
n	0	1	0	1
ω^*	1.5	1.5	1.5	1.5
z^*	1	1	1	1
D_p	0	0	0.1	0.1
D_n	1.92	439.15	1.61	396.96
$z_{initial}$	0	0.02	0	0.02
$\dot{z}_{initial}$	0	0	0	0

3.4. COMPARISON WITH ANALYTICAL MODEL

Another validation besides convergence test mentioned in Section 3.3 is made by driving an analytical model based on harmonic balance assumptions and comparing them with the numerical results. The harmonic balance is a well known method for finding solutions of

complex analytical models which is based on rewriting the given equation with the combination of sines and cosines. As you increase the sine-cosine numbers of the assumed equation, you converge to the exact solution more and more. To adopt this method to our model, both of the following two harmonic balance assumptions are employed:

$$z(t) = A\cos(\omega t) + B\sin(\omega t) \tag{3.1}$$

$$z(t) = A\cos(\omega t) + B\sin(\omega t) + C\cos(3\omega t) + D\sin(3\omega t) \tag{3.2}$$

Equation 3.1 represents the 2-term analytical solution assumption whereas Equation 3.2 represents the 4-term analytical solution assumption of the relative displacement motion equation of PM. It should be noted that, according to harmonic balance theory, we know that Equation 3.2 should give more accurate results than Equation 3.1.

In order to exemplify the implementation of harmonic balance method into derived harvester model, the work done for 2-term analytical solution for second order nonlinear system is shown below. Firstly, the first and second derivatives of the Equation 3.1 are taken as:

$$\dot{z}(t) = -\omega A\sin(\omega t) + \omega B\cos(\omega t) \tag{3.3}$$

$$\ddot{z}(t) = -\omega^2 A\cos(\omega t) - \omega^2 B\sin(\omega t) \tag{3.4}$$

After that, the equation of motion as it is seen in Equation 2.8 is rewritten with the assumptions made above. By grouping sine and cosine terms together in the resulting equation, we are able to get following two equations:

$$-\omega^2 mA + kA - \omega D_2 z^2 B + \omega D_p B = m\omega^2 Y_0 \tag{3.5}$$

$$-\omega^2 mB + kB - \omega D_2 z^2 A + \omega D_p A = 0 \tag{3.6}$$

Meanwhile, the nonlinear term of $D_n|z|^n\dot{z}(t)$ appeared in Equation 2.8 is rearranged by implementing Equation 3.1 into itself:

$$D_2(z)^2 z(t) = D_2[A^2cos^2(\omega t) + B^2sin^2(\omega t) + 2ABcos(\omega t)sin(\omega t)] \qquad (3.7)$$

Finally, after driving Equation 3.5, Equation 3.6 and Equation 3.7, sine and cosine terms are grouped all together to which gives:

$$-\omega^2 mA + kA + \omega D_p B - \frac{\omega A^2 B D_2}{4} + \frac{\omega B^3 D_2}{4} - \frac{\omega A^2 B D_2}{2} = m\omega^2 Y_0 \qquad (3.8)$$

$$-\omega^2 mB + kB + \omega D_p B - \frac{\omega A^3 B D_2}{4} - \frac{3\omega AB^2 D_2}{4} + \frac{\omega AB^2 D_2}{2} = 0 \qquad (3.9)$$

When we solve Equation 3.8 and 3.9 together, we are able to get the unknown terms "A" and "B" and the model becomes solvable.

To be able to implement these assumptions to our simulation model and run calculations, a certain script is written on MATLAB. This exact code and its related functions can be seen in Appendix B.

For the validation purpose, the numerical results for second order nonlinear system ($n = 2$) without parasitic damping case ($D_p = 0$) is chosen because of its higher nonlinearity order compared to other cases. The script written for validation is run with this scenario's parameters and the results of the analytical model are compared with the results of the numerical model.

In Figure 3.14 the percent difference of 2-term assumption analytical solution results with respect to numerical solutions graph is shown. It can be seen that the distribution of deviation of these two cases are different through the testing range. There seems to be a higher error in the region bounded by $0.4 < \omega^* < 0.8$. Rest of the regions is look like give relatively lower errors.
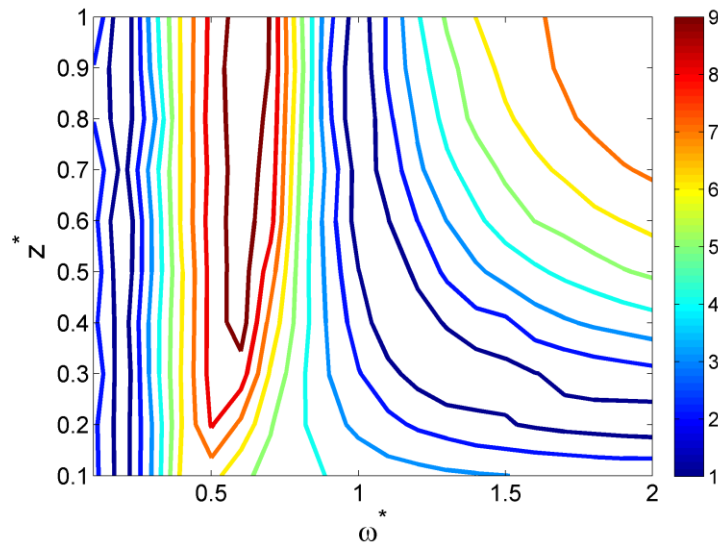
Figure 3.14. Percent difference of 2-term assumption results from numerical results
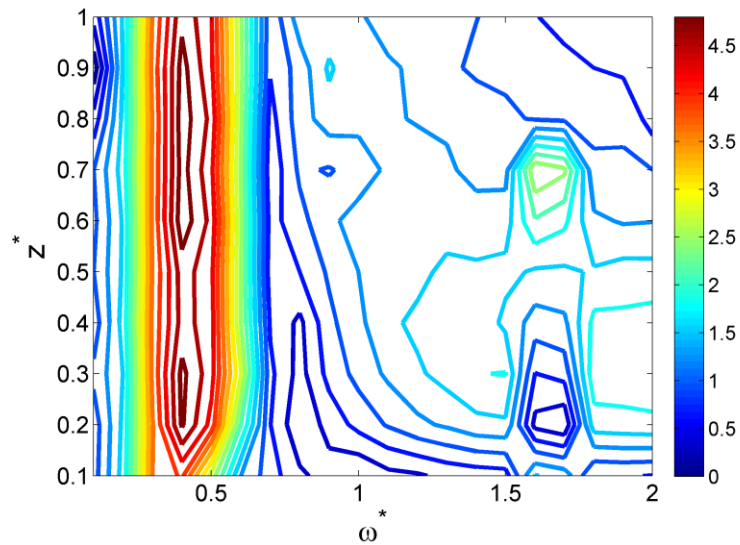
Figure 3.15. Percent difference of 4-term assumption results from numerical results

Figure 3.15 shows the percent difference of 4-term assumption analytical solution results with respect to numerical results. The distribution of errors map look like more or less the same with 2-term assumption model. The maximum error region is between the boundaries of $0.3 < \omega^* < 0.6$. It is important to see that the main difference of these two results is that the maximum error obtained by the 4-term assumption seems to be lower than the 2-term assumption model.

Table 3.3. Validation test results ($n = 2$)

	Max. Difference (%)	Avg. Difference (%)
2-term Assumption	9.82	4.11
4-term Assumption	4.99	1.65

Table 3.3 indicates and summarizes the results of these two assumption cases. It is seen that the average error found by 2-term assumption is 4.11 % while it is 1.65 % for 4-term assumption which can be considered as a significant decrease. The same amount of decrement can be seen in maximum difference values either. From that result we can conclude that as the term number of assumption increases, in other words, as the precision of analytical model increases, the results converge to the numerical solutions. It can be concluded that the numerical solutions that we have made is precise enough and acceptable amount of computational error exists.

3.5. DISCUSSION & SUMMARY

The computational study made for the proof of concept purpose of nonlinear damping proposition is presented in Chapter 3. The strategy chosen is to choose two different scenarios, with and without parasitic damping cases and test three different damping profiles namely; zeroth order, first order and second order damping profiles with these scenarios and other assumptions that have been made. The results are presented in the form of individual comparison plots.

When we look at non-parasitic damping scenario case, it is clearly seen that there is a noticeable amount of efficiency increment with the nonlinearity of the system. Although small regions of the testing ranges reveals some superiority of the linear damping system, it can be concluded that, theoretically it is proven that using nonlinear damping within the boundaries of an energy harvester increases its efficiency. Also it can be said that, the nonlinear damping increases the optimum region range that the harvester can work. This can be considered as another approval of the proposition. Another conclusion that we can come up is that as we increase the nonlinearity, the efficiency increment increases under ideal circumstances. All of these results can be considered as promising outcomes.

If we look at the second scenario, non-parasitic damping case, it can be seen that the amount of parasitic damping that the device has a big influence on the effectiveness of the proposed system. According to results, it can be concluded that, as the parasitic damping goes higher, the efficiency increment we can get by using a nonlinear damping profile goes lower. After a certain amount, the linear and nonlinear systems seem to have no difference and there is even a superiority of linear systems over proposed systems. Since most of the energy harvesters are being produced in MEMS scale, they have different dynamical characteristics and it is predicted that the harvester will not have high loss because of an existence of a parasitic damping. Nevertheless, this should be considered as a outcome to keep in mind.

Finally, one can say that the proposition of using nonlinear damping is proven to be promising theoretically. The nonlinearly damped systems increase power that can be harvested from the environment and increases the feasible range that the harvester can work efficiently.

4. PHYSICAL REALIZATION OF NONLINEAR DAMPING

After the computational analysis and finding promising results with nonlinear damping, an experimental study is done in order to show that a nonlinear damping profile can be realized in a real system. For that purpose, an experimental setup is designed and built and set of experiments are performed. This chapter presents the work for physical realization of nonlinear damping.

4.1. GENERAL DESCRIPTION OF EXPERIMENTS

After numerically validating the advantage of nonlinear damping, the scope of the experimental study is chosen as proofing the feasibility of creating a nonlinear distribution of electrical damping profile along the travel span of a PM according to design requirements.

To be able to accomplish creating nonlinear damping profile goal, the physics of interaction between coils and a permanent magnet should be used. As Faraday's Induction Law suggest, if a conductor is exposed to a varying magnetic field, potential difference across itself is produced. In other words, if a magnet is forced to move inside of a certain wire loop with a specific speed, voltage difference occurs between the two ends of the conducting wire. The voltage generated within a tightly wounded coil wire is formulated as:

$$\varepsilon = -N\frac{d\Phi_B}{d_t} \tag{4.1}$$

where ε is the EMF (electromotive force) in Volts, Φ_B is the magnetic flux in Webers and N is the number of loops.

In order to predict the amount of damping effect of the electromagnetic field on the moving magnet, firstly the coupling between the mechanical and electrical governing equations has to be determined. The mechanical equation can be written as[13];

$$\ddot{z}(t) + 2\zeta_p\omega_\mathrm{n}\dot{z}(t) + \omega_\mathrm{n}{}^2 z(t) - \frac{\Theta}{m}I = \frac{F(t)}{m} \tag{4.2}$$

where "I" is the electrical current in units of Ampere and "$F(t)$" force exerted on the mass in units of Newton. In that equation, the term Θ represents the coupling factor and equals to the EMF over magnet speed i.e. $\Theta = \varepsilon/v$ [13]. Meanwhile the electrical governing equation can be written as:

$$L\dot{I} + (R_L + R_I)I + \Theta\dot{z} = 0 \tag{4.3}$$

where L, R_L and R_I represents inductance, external load resistance and internal resistance respectively. It should be noted that in this experimental study, it is decided to work with relatively low coil turn numbers so that the inductance term appearing in Equation 4.3 can be neglected (i.e. the inductance calculated for 200 coil turns result as 7.61 mH). If we do that and leave I term alone in this equation, it becomes as it is shown in Equation 4.4.

$$I = -\frac{\Theta\dot{z}}{R_L + R_I} \tag{4.4}$$

Now if we combine Equation 4.4 and Equation 4.2 together and rearrange, we will be able to get a full representation of the system in a single equation. The resulting equation becomes:

$$m\ddot{z}(t) + (2\zeta_p m\omega_\mathrm{n} + \frac{\Theta^2}{R_L + R_I})\dot{z}(t) + kz(t) = F(t) \tag{4.5}$$

When Equation 4.5 is examined, it can be seen that the electrical damping term is linearly dependent on the square of the coupling coefficient. All the other terms that affect damping can be considered as constant. This situation leads us to conclude that if we can compute Θ^2 value from the experimental results, it will be enough for obtaining the change in damping

with respect to mass displacement. As a result of this conclusion, it is decided to measure the voltage changes of each individual coil over time during experiments and calculate square of coupling coefficient for each data sampling to plot the damping profiles as it is seen in Equation 4.6.

$$\Theta_n{}^2 = \frac{\varepsilon_n{}^2}{v^2} \tag{4.6}$$

4.2. DESIGN OF EXPERIMENT

For the purpose of modeling the relationship between the electrical damping and coil arrangements, it is seen that a unique experimental setup is necessary so that the conductor coil arrangements can be made and the speed of a certain magnet that passes through the loops can be adjusted. This section of the report describes the experimental setup and procedure.

4.2.1. Methodology

The brief flow path of the planned methodology for the experimental study is as follows:

   i.   Design and build an experiment setup that allows trying different coil arrangements and magnet speeds.
  ii.   Install necessary equipment for the purpose of collecting data.
 iii.   Make initial experiments with different number of coil loops and record the voltage profiles to be able to characterize system.
  iv.   Create an empirical relationship between the number of coils and the damping
   v.   Determine a linear and nonlinear damping profile to achieve.
  vi.   Develop an algorithm by the help of the empirical relationship to predict the necessary coil numbers to get the determined damping profiles.
 vii.   Handle final experiments to validate the goal accomplishment of having desired profiles.

More verbally, first of all an experimental setup is built that allows trying different coil numbers and collecting the voltage data with respect to time to be able to calculate the damping profile. After performing initial experiments with the known number of coil loops certain damping profiles is selected to be obtained. The selected profiles can be seen in Figure 4.1. Figure 4.1.a shows a linear damping profile that corresponds to conventional energy harvesters and Figure 4.1.b. shows a nonlinear profile which is a representative of nonlinear damping proposition.

| (a) | (b) |
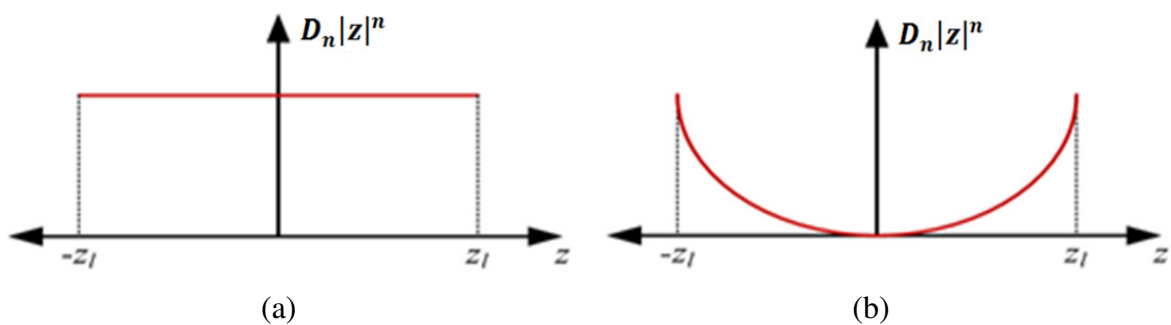
Figure 4.1. Selected damping profiles **(a)** linear profile **(b)** nonlinear profile

To be able to obtain profiles shown above, it is aimed to develop an algorithm that uses the initial experiment data and estimates the coil loop arrangement that converges to the desired profile. Finally, it is planned to handle a final set of experiments to validate the compliance of the calculated coil arrangement with the real physical system results.

4.2.2. Experiment Setup Design

As mentioned in previous sections, the planned experimental setup should have three important specifications:

    i.   Variable coil loop adjustment

    ii.   Speed control for the magnet

    iii.   Data acquisition

In the design stage, solid drawings of the complete system are made. Before explaining the parts individually, the overall designed system is shown in Figure 4.2.
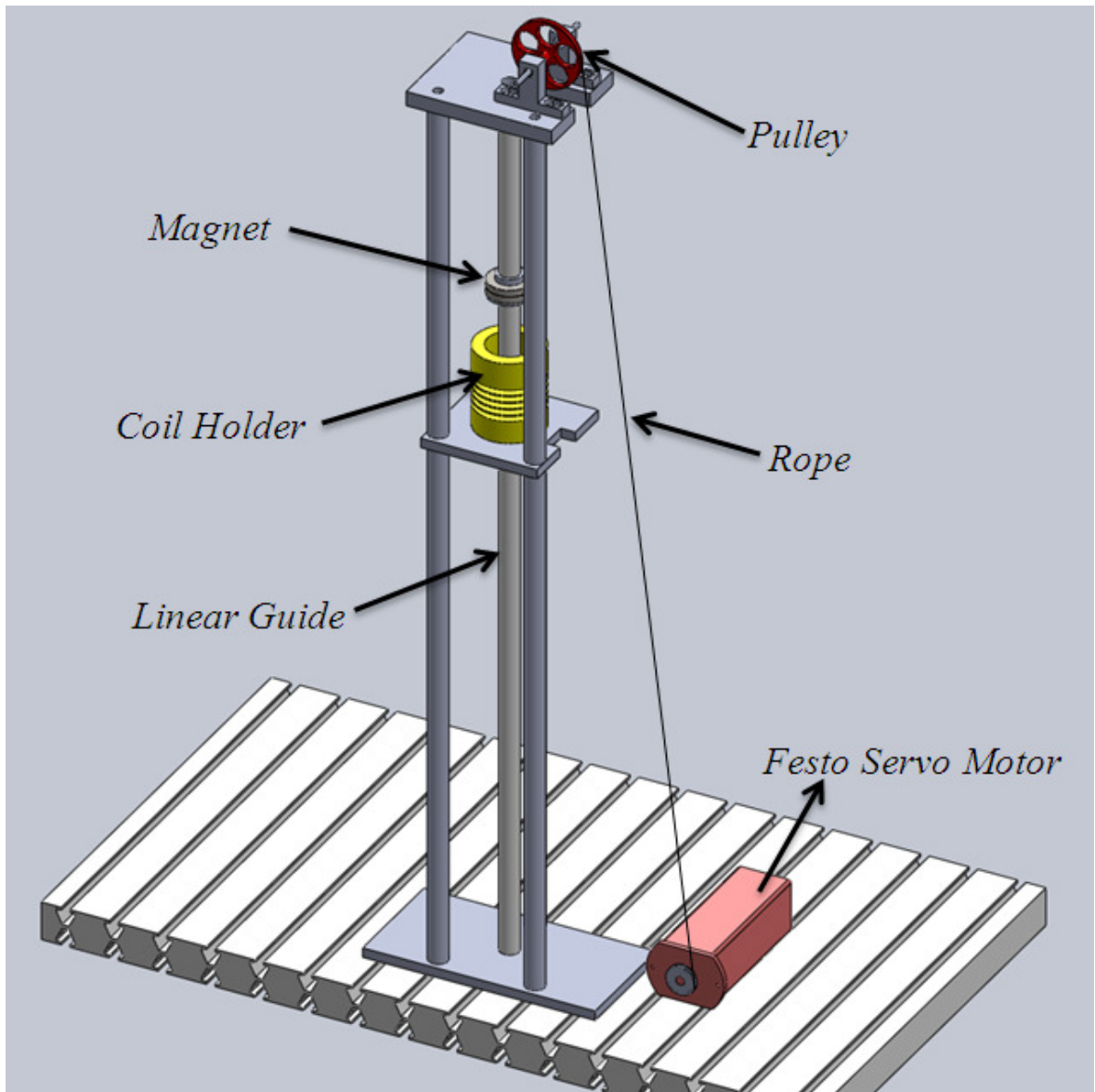
Figure 4.2. Solid drawing of the complete experimental setup

As can be seen in Figure 4.2, the magnets are guided with a linear guide vertically is placed in the middle of a main carrying structure. The selected magnets are two N38 type neodymium magnets placed successively(see Figure 4.3). The magnetic properties and dimensions of the magnets are shown in Table 4.1.
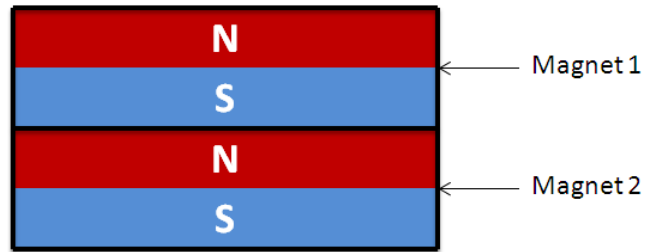
Figure 4.3. Magnet configuration

Table 4.1. Properties of the selected magnets

Type	N38
Outer Diameter (mm)	44
Inner Diameter (mm)	27
Height (mm)	7
Residual Flux Density (Kgs)	12.4
Coercive Force (KOe)	11.0
Instrinsic Coercive Force (KOe)	12.0
Max Energy Product (MGOe)	36

The magnets are connected to a FESTO servo motor by the help of a pulley and rope. The starting point of the magnets are planned to be near the lower end of the linear guide. The Festo Servo Motor with a motor controller pulls the magnet up with a given constant speed and as a result, the magnets go through the coil holder to induce voltage. After that, magnets stop near the upper end of the linear guide. The point of stop is determined by the motor controller with the help of a placed inductive sensor.

The perspective view of the coil holder can be seen in Figure 4.4. Since the planned experiment procedure requires the ability to try different coil arrangements, the section where the conducting wire is going to be placed is divided into five separate regions. By this way, it is aimed to be able to create a nonlinear distribution of coil turns to get the desired damping profile. The material selected to be used to manufacture the coil holder is cast polyamide since it is nonmagnetic. The detailed dimensions of the part can be seen in Figure 4.5.
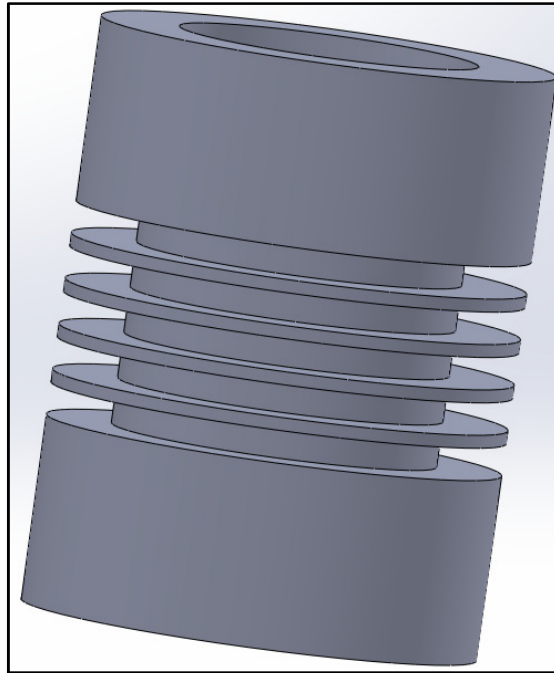
Figure 4.4. Perspective view of the coil holder
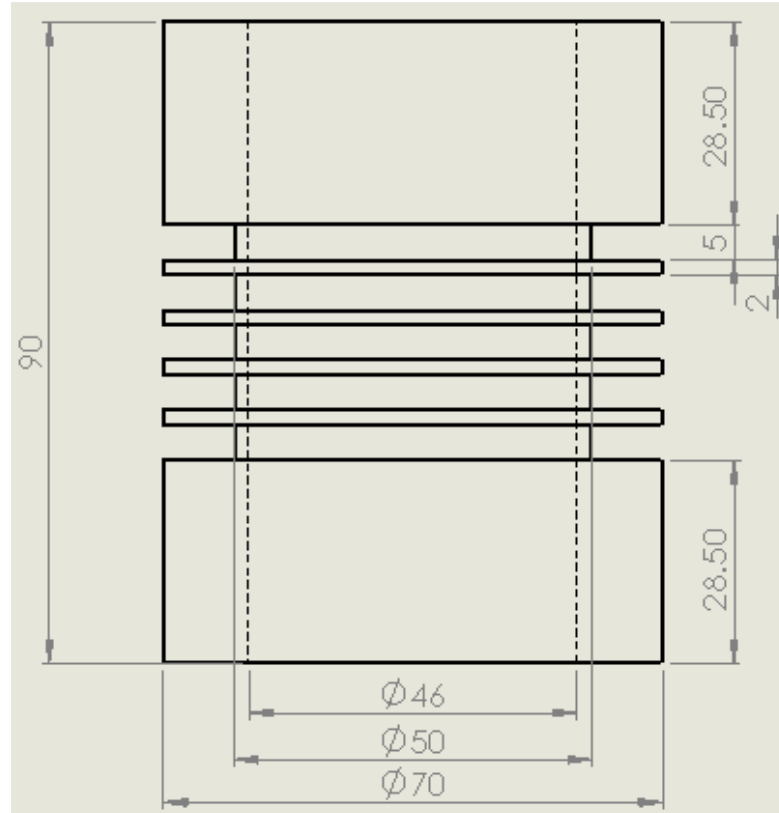
Figure 4.5. Dimensions of the coil holder (dimensions in mm)

The coil loops wrapped around the coil holder are connected to a National Instruments Data Acquisition Card separately. By this way, the voltage of each coil with respect to time can be measured. At the initialization and calibration stage of the experiments, it is seen that data acquisition rate of 5 kHz is good enough to capture the voltage data with high resolution.

During the experiments, it is decided to keep the magnet speed fixed to maintain consistency for all trials. The selected speed is 205 mm/s that correspond to 250 RPM rotational speed of the servo motor.

After all design stages are completed, the parts are manufactured and assembled. The fully assembled system is shown in Figure 4.6 and Figure 4.7.
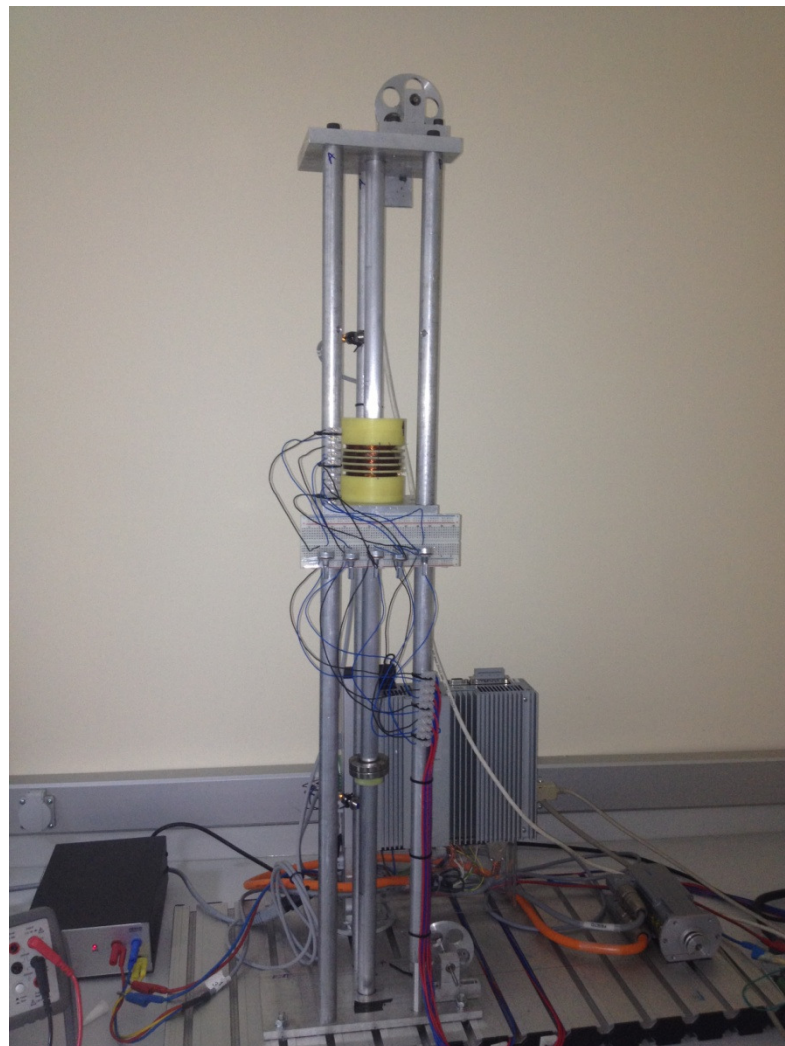
Figure 4.6. Experiment setup view
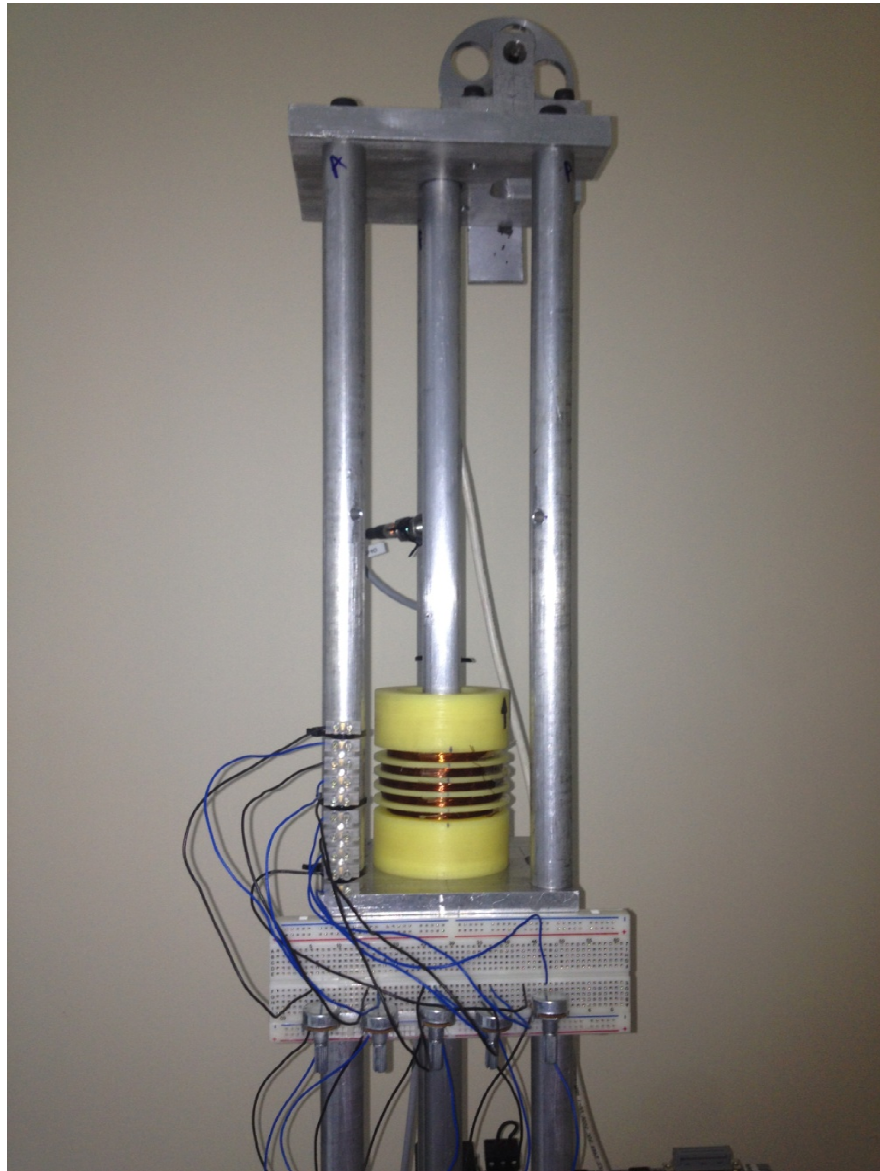
Figure 4.7. Coil holder detailed view

4.3. EXPERIMENT RESULTS AND DISCUSSION

Firstly, it is aimed to determine the basic characteristics of the system such as the effect of magnet speed and number of coil loops on the voltage output of the system. After that a certain optimization algorithm that uses the initial experimental data is implemented in order to predict the required coil arrangement for the system to achieve desired damping profiles. At the final stage of the experimental study, the coil arrangements calculated by

the algorithm are tested on the setup and the actual damping profiles are compared with the desired damping profiles. This section of the thesis report gives the results of these studies.

4.3.1. Effect of Speed Tests

For the purpose of initial characterization study of the setup, firstly the effect of magnet speed on the open circuit voltage output of the system is determined. For this task, one coil holder is wounded with 200 coil turns and the magnet is driven through it for nine different speed values by using Festo servo motor. The voltage output of the coil with respect to time is acquired by the data acquisition box with 5 kHz sampling rating frequency.
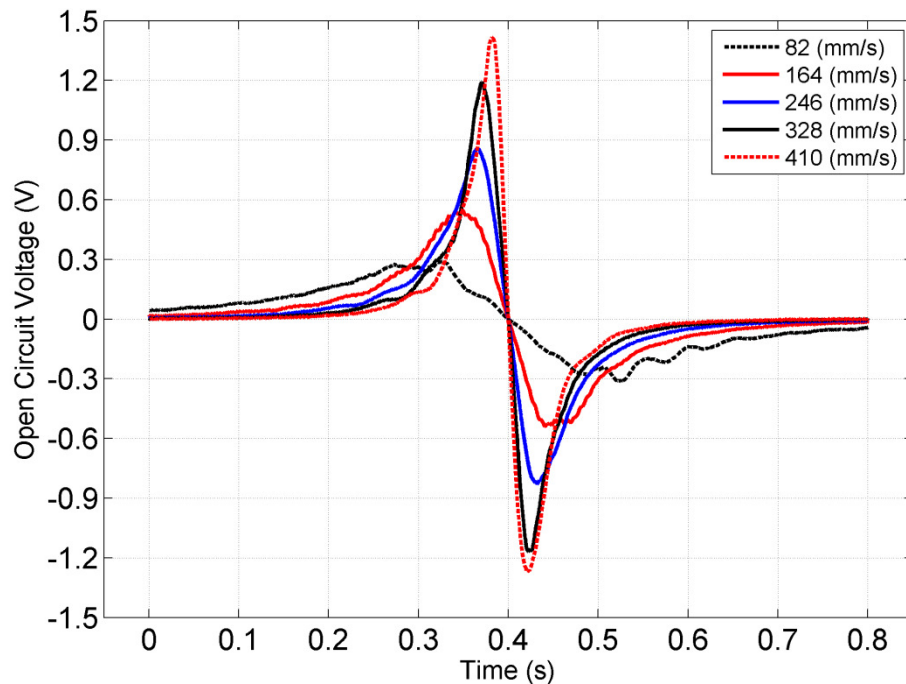
Figure 4.8. Plot showing the effect of magnet speed on the open circuit voltage

The Figure 4.8 shows the results for five different speed values that are 82, 164, 246,328 and 410 mm/s. The horizontal axis and vertical axis indicates the time in seconds and open circuit voltage output of the coil in volts respectively. Firstly, it can be said that the voltage profile of the coil came out as it is expected. It goes to a positive maximum value as the magnet approaches to the coil, than it goes down to zero when the magnet is just in the middle of the coil and it goes further down to negative minimum voltage as the magnet

moves away. If we look at the positive maximum voltages it is seen that as the magnet speed increases, the maximum voltage value increases, which is again an expected result.

Table 4.2. Maximum voltages for different speeds

Speed (mm/s)	Maximum Positive Voltage (V)
82	0.289
123	0.418
164	0.562
204	0.688
246	0.829
286	0.956
328	1.111
368	1.235
410	1.374

Table 4.2 reveals the measured maximum voltages for different speed trials. From this table it is again seen that as the speed increases the maximum voltage increases. It can also be concluded that there is a linear relationship between the maximum voltage and the magnet speed i.e. as we double the speed of magnet, the maximum voltage doubles. This gives us an idea that if we know the number of coil turns, we can predict the resultant voltage profile for the given speed value for our system.

4.3.2. Effect of Number of Coil Turns on the Open Circuit Voltage

After determining the speed effect on the voltage outputs, the effect number of coil turns is decided to be determined. For that purpose, it is selected to keep the magnet moving speed constant at 204 mm/s which corresponds to the 250 RPM of the driving servo motor. Three different numbers of coils are wounded to the coil holders. The selected coil turn numbers are 50 turns, 100 turns and 150 turns. After the experimental setup is ready, the voltage outputs of the coils are collected with the data acquisition system with 5 kHz sampling rating frequency.
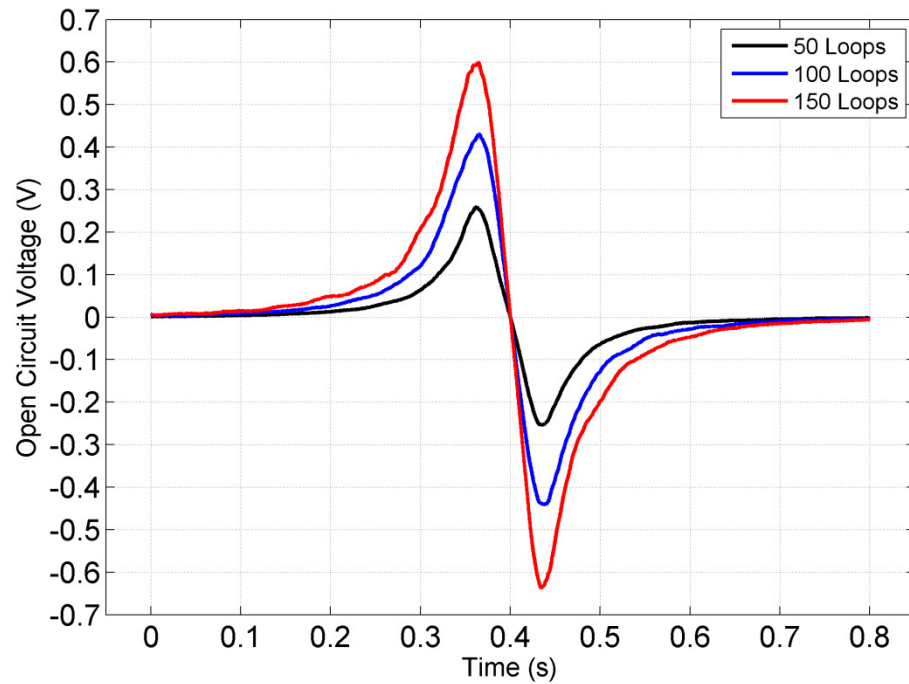
Figure 4.9. Plot showing the effect of number of turns on open circuit voltage

The Figure 4.9 shows the results of the three different experiments plotted on the same graph. The horizontal axis and vertical axis indicates the time in seconds and open circuit voltage of the coil in volts respectively. It can be observed that the results came out as they are expected again. As the number of coil loops increases the amplitude of voltage of the coil increases and again it can be said that there is a linear relationship between the number of coils and open circuit voltage.

4.3.3. Damping Profile Finder (DPF)

After finding out that a model can be created for predicting the voltage output of the coils for different magnet speeds and coil loops values, it is decided to construct an algorithm that calculates the coil arrangements for obtaining desired damping profiles. For that purpose an algorithm is developed, which is called "Damping Profile Finder" (DPF). The flow chart of the algorithm can be seen in Figure 4.10.

The DPF algorithm can be briefly described as follows. Firstly, it creates the displacement vs. damping constant vector that corresponds to the desired damping profile. Then, by using the empirical model created previously, it predicts the open circuit voltages of all coils by making interpolations using all possible configurations of five coils. Again for all coil arrangements the total damping profiles are calculated and recorded to a resultant matrix. At the end, all of the damping profile results are compared with the desired damping vector by using least square method. The best damping profile fit among them is reported as the coil arrangement to be used for obtaining the desired damping profile.

The script of the DPF and its associated functions are given and can be seen in Appendix C.

The DPF script is run for two cases. For the first case a linear damping profile within the range of -20 mm to +20 mm along the travel span of the magnet is planned to be created. For the second case, creating a nonlinear damping which is intended to be representing the second order nonlinear damping case is chosen. Since we have five separate coil holders within the experimental setup, they are given numbers to prevent confusion, i.e. +2, +1, 0, -1, -2 starting from the top coil holder to the bottom one. Thus, the coil holder number "0" corresponds to the coil right at the middle of the travel span. The resultant coil turn numbers calculated by the DPF algorithm is forced to be symmetric around coil holder "0". i.e. the required numbers are calculated for coil holders number +2, +1, 0 and rest of the holders are assumed to be symmetric with the upper part.

It should be noted that the number of turn values are constrained within a range (50 turns – 400 turns) to avoid results with the negative turn numbers and positive but small turn numbers.

,
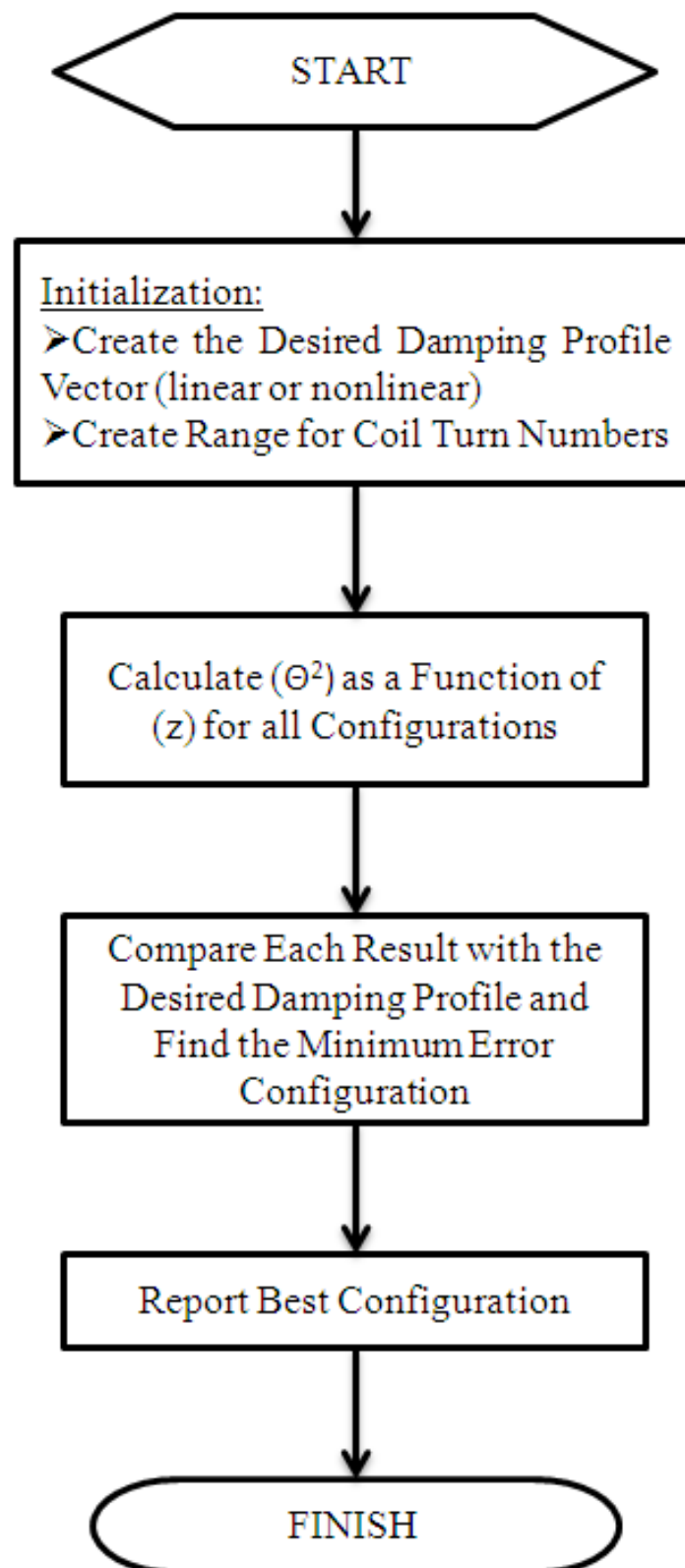
Figure 4.10. Flowchart of DPF

Figure 4.11 represents the results of DPF algorithm that is run for obtaining linear case scenario. The upper plot shows the calculated open circuit voltage of each coil with respect to the magnet displacement $z(t)$. $z(t) = 0$ corresponds to the position where the magnet structure is at the middle of coil 0 (middle coil). The lower part of the figure shows the desired damping profile and fitted square of coupling coefficient, θ^2 which represents the resulting damping profile on the same plot. While plotting this figure, the coupling coefficient profiles are calculated individually for each coil as it is seen in Equation 4.3. After that, the results for all five coils are added together to obtain final resulting damping profile. This same method applies to all following damping profile graphs presented in this chapter. The corresponding coil arrangement obtained that fits best to the given linear desired damping profile is shown in Table 4.3.
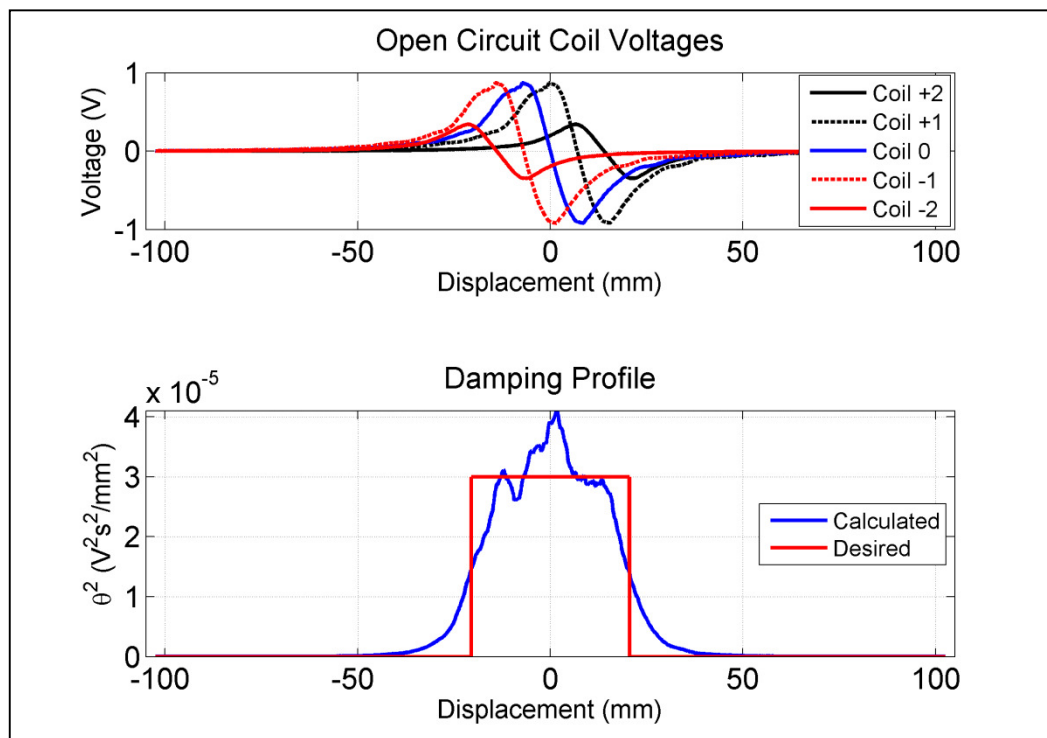
Figure 4.11. Calculated damping profile for linear scenario

In the Figure 4.11, it is seen that the desired damping profile is partly achieved with DPF script. The reason for not being able to get a better fit is predicted to be because of having five discrete coil holders in the coil winding region. Increasing the coil holder number and

decreasing their height would increase the fitness of the results. However this would result in an increase in system complexity.

Table 4.3. Number of coil loops for linear case

Coil Number	Number of Coil Turns
Coil +2	100
Coil +1	254
Coil 0	302
Coil -1	254
Coil -2	100

Figure 4.12 shows the results for nonlinear case scenario. Again the upper part of the figure shows the calculated voltage outputs of each coil with respect to magnet displacement and the lower part of the figure shows the desired damping profile and calculated damping result on the same plot. The number of coil loops obtained by the code is shown in Table 4.4. It should be noted that the found number of coil loops by DPF is intended not to be below 50 turns because of the voltage reading range purposes. The coils loops below that value gave very low voltage outputs and they were below the reading range of the data acquisition system.
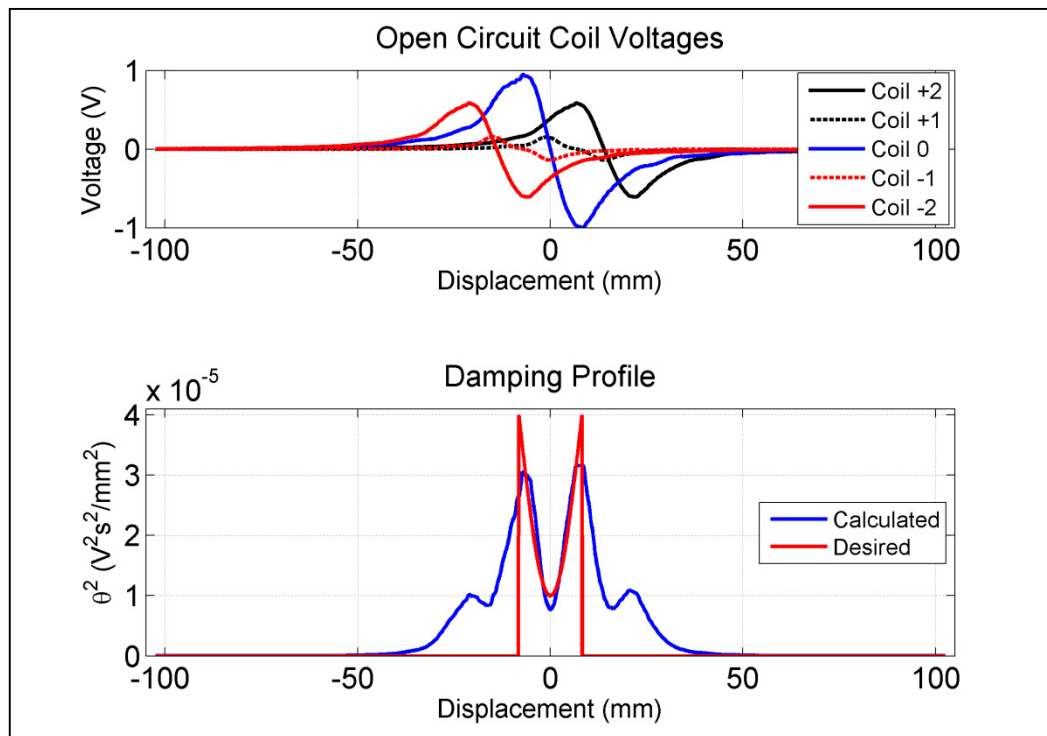
Figure 4.12. Calculated damping profile for nonlinear scenario

When we examine Figure 4.12, it can be said that the obtained damping profile nicely fits to the desired damping profile. Especially near at the point of interest region where magnet displacement is between +8 mm and -8 mm we were able to get fine results. Again, widening the [-8 mm +8 mm] range results in increased discrepancy due to the limitations of the system.

Table 4.4. Number of coil loops for nonlinear case

Coil Number	Number of Coil Turns
Coil +2	194
Coil +1	69
Coil 0	296
Coil -1	69
Coil -2	194

It should be noted that if the calculated turn numbers for desired damping profiled is scaled up or down with an integer, the resultant damping profile scales up or down with the same scale. There wouldn't be any change in the profile.

After simulating the two separate scenarios and finding the best possible damping profiles that fits to desired ones, experiments are made to see if it is possible to obtain the same results with the simulated ones or not. The work that has been done for this purpose is presented in the next section.

4.3.4. Physical Realization of the Damping Profiles

As a final part of the experimental study, the simulated damping profiles are validated experimentally.

For the first, linear damping case scenario, the coil holders are coiled up with the numbers found with DPF i.e. 100-254-302-254-100. The wound coils are then connected to the data acquisition system separately. The speed of magnet is adjusted to 204 mm/s which is the same value used in DPF script. The data sampling rate is set to 5 kHz. The results of the experiment are shown in Figure 4.13.
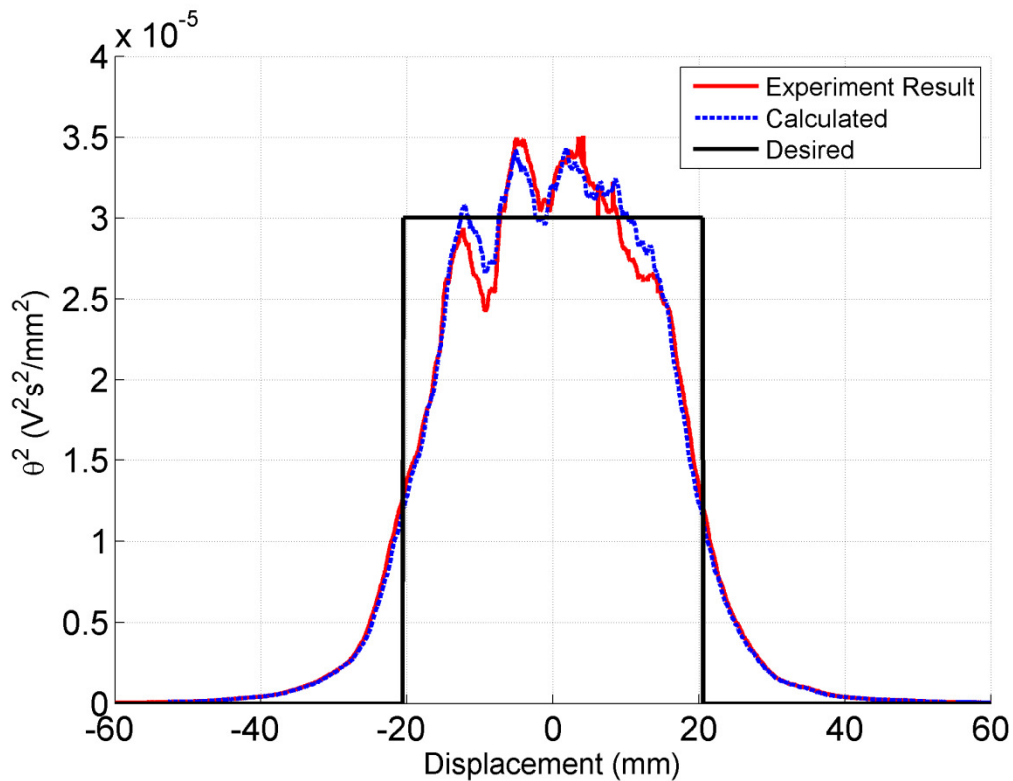
Figure 4.13. Experiment result of linear damping scenario

In Figure 4.13, red, dashed blue and black lines represent the experimental damping results, damping results calculated by DPF and desired damping profile, respectively, with respect to magnet displacement. As seen from the figure, the DPF result closely follows the experimental result. Calculated relative standard deviation found as around 10.6 %. This gives us an initial idea of success of the developed DPF code.

After repeating this experiment several times, coils are removed and the coil holders are coiled up again with the arrangement found for nonlinear damping profile i.e. 194-69-296-69-194. The system is again connected to the data acquisition box with 5 kHz sampling rate and magnet speed is again adjusted to the 204 mm/s.

The results found for this scenario are presented in Figure 4.14. Again in this figure the red, dashed blue and black lines represent the experimental damping results, the damping results calculated by DPF and desired damping profile respectively with respect to magnet displacement. Again the results show that the DPF successfully calculated the turn

numbers that give the desired damping profile. The experimental result is almost exact with the calculated values. This success reinforces the reliability of the DPF algorithm.
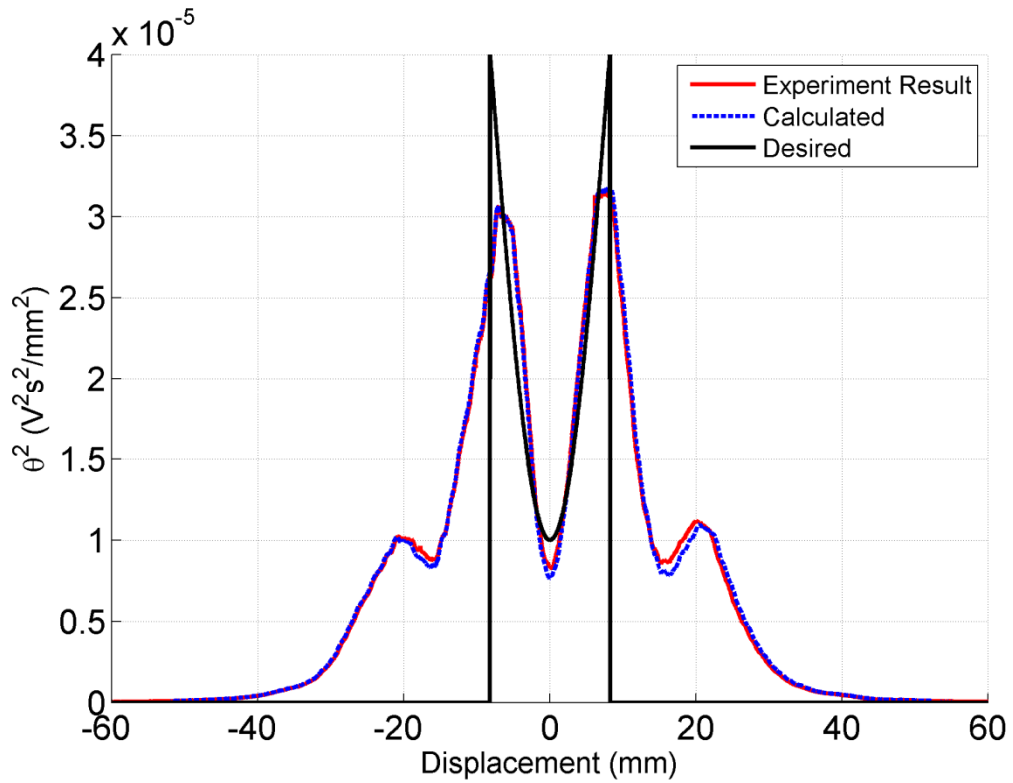
Figure 4.14. Experiment result of nonlinear damping scenario

Finally, after validating the two damping profile cases, it can be concluded that simulating the required arrangement for obtaining a required damping profile is achievable. By having higher number of coil regions with less height, it is possible to obtain better results. This can be noted as a future work to be done.

5. CONCLUSION AND FUTURE WORK

In this thesis work, the effect of using nonlinear electrical damping on the efficiency of energy harvesters and physical realization of nonlinear damping is presented.

Firstly, the numerical analysis have been made for three different damping profiles, i.e. zeroth order linear damping, first order nonlinear damping and second order nonlinear damping profiles. These profiles are analyzed, i.e. nonparasitic ($\zeta_p = 0$) and parasitic ($\zeta_p = 0.01, 0.1, 0.5$) cases. For each cases and damping profiles, the models are tested within $0 < z^* < 1.0$ and $0 < \omega^* < 2.0$ testing range. While making a calculation for a single ($z^* - \omega^*$) pair, the required damping for the system is calculated so that the extracted power is maximized by the help of DCOS subroutine. The power results are nondimensionalized for the sake of comparison purpose.

When we look at the individual nondimensionalized power results of three different damping profiles for $\zeta_p = 0$ scenario, we can come up with the following conclusions listed below:

- All of three damping profiles seem to have same pattern over the given ($z^* - \omega^*$) ranges.
- The maximum power region is around the resonant line ($\omega^* = 1$), which is an expected situation.
- All three systems faces with dramatic efficiency loss below the value of $\omega^* = 0.5$.
- As the degree of nonlinearity increases, some changes appear to be occur in nondimensionalized power results.

When a comparison is made between the zeroth order linear system and other two nonlinear systems, the following conclusions are reached:

- At the first look, it can be said that as the degree of nonlinearity increases, the efficiency of the system increases in majority of the testing range.

- The main efficiency increment appears to be located within the $0.4 < \omega^* < 1.5$ range.

- For both $n = 2$ and $n = 1$ systems, the maximum efficiency increase occurs slightly below the resonant line ($\omega^* = 0.7$). Again for both profiles, linear damping system seems to have same performance with nonlinear damping systems below the line of $\omega^* \leq 0.3$. Moreover, linear system comes up with better performance in the region bounded by $\omega^* > 1.4$ and $z^* > 0.5$.

- If we look at the percent difference results, it can be concluded that the maximum efficiency increase that can be get with first order nonlinear system is around 10 % while it is around 15 % compared with zeroth order linear system.

- In the relatively small regions where linear system gives better efficiency, the maximum efficiency difference is around 2 % when we compare it with $n = 1$ case and it is 6 % when compare it with $n = 2$ case.

- To sum up, it can be said that as the degree of nonlinearity increases, the efficiency of the system increases in majority areas of the testing range. This results in being able to extract more power from the environment and increasing the working range that the harvester works optimally.

For the second part of the numerical analysis study, parasitic damping is added to the simulations to see the effect of external losses due to friction or etc. In order to do that, three different levels of parasitic damping is selected ($\zeta_p = 0.01, 0.1, 0.5$). When the percent difference results of nonlinear systems with respect to linear system is analyzed, the following results are obtained:

- At the first sight, it can be seen that as the level of parasitic damping increases, the level of efficiency increase decreases for both first and second order nonlinear systems.

- The regions where nonlinear damping cases are giving better results starts to shrink with the increase of parasitic damping.

- The maximum efficiency increase that can be get with first order nonlinear system goes down from 10 % to 8 % and from 8 % to 6 % as the parasitic damping increases from $\zeta_p = 0.01$ to $\zeta_p = 0.5$.

- The maximum efficiency increase that can be get with second order nonlinear system goes down from 12 % to 9 % and from 9 % to 5 % as the parasitic damping increases with the same order.

- When the amount of parasitic damping raises from $\zeta_p = 0.01$ up to $\zeta_p = 0.5$ the nonlinear systems seems to lose their superiority compared with linear system.

- As a result, it can be concluded that, the level of parasitic damping has a big influence on the success of nonlinear damping proposal.

At the final stage of the numerical analysis, the results are validated by using analytical harmonic balance method. For that purpose, the theoretical model of second order nonlinear system with nonparasitic damping case is tested with two different harmonic balance assumptions, i.e. 2-term assumption and 4-term assumption. As a results it is seen that;

- The maximum difference between the harmonic calculation and numerical results is 9.82 % whereas it is 4.11 % in average for 2-term assumption. $(z(t) = A\cos(\omega t) + B\sin(\omega t))$

- On the other hand, the maximum difference between the harmonic calculation and numerical results is 4.99 % whereas it is 1.65 % in average for 4-term assumption. $(z(t) = A\cos(\omega t) + B\sin(\omega t) + C\cos(3\omega t) + D\sin(3\omega t))$

- As the number of terms of the assumption increases, the harmonic results approaches to the numerical results.

- The numerical results can be considered to match with the results of the harmonic balance method.

Finally, the physical realization of the nonlinear damping system is decided to be made experimentally. For that purpose the electrical and mechanical model of the system is driven and an appropriate experimental setup is built. The first experiments are done to characterize the system. After that, an appropriate algorithm is developed to find out the required coil configuration for obtaining desired damping profiles empirically. Finally, the required coil arrangements are calculated for two different damping profiles and the results are tested experimentally. It is seen that for both linear and nonlinear damping profile

cases, the desired damping profiles appeared to be almost exact with the calculated damping profiles.

To sum up, it this thesis work, it is numerically shown that an efficiency increase can be obtained with nonlinear damping profiles. The range that an energy harvester works optimally can be increased with a properly designed nonlinear energy harvester. It is also shown that, a desired nonlinear damping profile can be empirically calculated and obtained for real physical systems successfully.

The selected topics for future work of this study are listed below:

- ***"Developing an analytical model for the equations of motion and power equations"***: Since all the calculations are made with numerical methods, driving an analytical model for the systems and recalculating the simulations would give better results.

- ***"Increasing the testing range of the computational study"***: Calculating the solutions for wider testing range would give a better idea of the behavior of nonlinearly damped systems.

- ***"Testing with higher order nonlinearity terms"***: The nonlinearity term can be increased further in computational analysis.

- ***"Making experiments that proof the efficiency increase of the nonlinear systems and validating analysis results"***: The effect of nonlinearity on the performance of energy harvesters should be validated experimentally.

- ***"Designing and building a better performance energy harvester for everyday use"***: Commercially available better performance energy harvester is the final goal of this study.

6. APPENDIX A: SIMULATION CODES

Algorithm A.1. Main function

```matlab
tic
clear all
clc
global yo
global eps
global w
global wc

zl=0.01;
zlyo_range=0.1:0.1:1;
yo_range = zl./zlyo_range;
wc_range = 0.1:0.1:2;

a=1;
for wc=wc_range
    [t_initial,t_final,m,k,n,zl] = inputs();
    eps_seed=100;
    b=1;

    for  yo = yo_range

        [eps,fval,exitflag]=fminsearch(@powerobjfun,eps_seed,
optimset('TolX',1e-3,'TolFun',1e-3));
        display(['eps calculated by unconstrained opt module is
',num2str(eps)]);
        [Power_temp,zmaxx] = trapezoidal(eps);
        Opt_matrix(a,b) = 1; % 1 means unconstrained opt.: REGION 1
        if (zmaxx(:,1)>=zl)
            display([num2str(zmaxx(:,1)),' is bigger than zl, which
is ',num2str(zl)]);

[eps,fval,exitflag]=fminsearch(@objfun,eps_seed,optimset('TolX',1e-
3,'TolFun',1e-3));
            display(['eps calculated by constrained opt module is
',num2str(eps)]);
            [Power_temp,zmaxx] = trapezoidal(eps);
            display([num2str(zmaxx(:,1)),' is now within the
limits']);
            Opt_matrix(a,b) = 2;
        end
        Eps_matrix(a,b) = eps;
        eps_seed=eps;
        Power(b)=Power_temp;%#ok
        zmax(b) = zmaxx(:,1);
        b=b+1;
    end

    for r=1:length(Power) %Mitcheson Normalization
        Power(r)=Power(r)/((yo_range(r)^2)*(w^3)*m);%#ok
        Results(a,r)=Power(r);
    end

    a=a+1;

    size (Results)
```

```
end

a=zl./yo_range;
toc
surf(a',wc_range',Results)
```

Algorithm A.2. trapezoidal.m function

```
function [P,z_max] = trapezoidal(eps)
global yo
[t_initial,t_final,m,k,n,zl] = inputs() ;

F = F_handle(eps);
[t,z] = ode45(F,[t_initial,t_final],[0,0]);

for i=1:length(t)
    INTEGRAND(i) = abs((z(i)^n*z(i,2)^2));
end;

INTEGRAL = trapz(t,INTEGRAND);
P=INTEGRAL*eps/(t_final-t_initial);
z_max = max(z);
```

Algorithm A.3. objfun.m function

```
function f = objfun(eps)

[P,z_max]= trapezoidal(eps);

[t_initial,t_final,m,k,n,zl] = inputs() ;

f = (zl-z_max(1))^2;
```

Algorithm A.4. powerobjfun.m function

```
function f = powerobjfun(eps)

[P,z_max]= trapezoidal(eps);

f = 1-P;
```

Algorithm A.5. F_handle.m function

```matlab
function h = F_handle(eps)
h = @real_F;
    function zp = real_F(t,z)
        global yo
        global w
        [t_initial,t_final,m,k,n,zl] = inputs();

        zp = zeros(2,1);
        zp(1)=z(2);
        zp(2)=((m*yo*w^2*cos(w*t))-k*z(1)-eps*abs(z(1)^n)*z(2))/m;
    end
end
```

Algorithm A.6. inputs.m function

```matlab
function [t_initial,t_final,m,k,n,zl] = inputs()
global w
global wc
n = 0;
zl = 0.01;
m = 0.02;
k = 120;
wn = sqrt(k/m);
w = wc*wn;
t_initial = (0*pi)/w;
t_final = (64*pi)/w;
```

APPENDIX B: SCRIPTS OF ANALYTICAL MODEL

Algorithm B.1. Main function

```
clear all
clc
tic
[t_initial,t_final,m,k,n,zl,wc,w,fourier_order,eps,zlyo_range] =
inputs();

x=zeros(fourier_order*2,1);

[x,fval,exitflag,output] = fminsearch
(@model,x,optimset('MaxFunEvals',100000000,'MaxIter',1000000))

%%single re-calculation with the found parameters to see the results
yo = zl./zlyo_range;

for ind=1:2:((fourier_order*2)-1)
    a(ind) = x(ind);
    b(ind) = x(ind +1);
end
time_step = 0.001;
t=t_initial:time_step:t_final;
z = zeros(length(t),1);
zdot = zeros(length(t),1);
zdotdot = zeros(length(t),1);
last_term = zeros(length(t),1);

for k=1:fourier_order
    i=1;
    for t=t_initial:time_step:t_final
        z(i) = z(i) + ((a(k)*cos(k*w*t)) +  (b(k)*sin(k*w*t)));
        zdot(i) = zdot(i) + (-a(k)*k*w*sin(k*w*t) +
b(k)*k*w*cos(k*w*t));
        zdotdot(i) = zdotdot(i) + (-a(k)*(k^2)*(k^2)*cos(k*w*t) -
b(k)*(k^2)*(w^2)*sin(k*w*t));
        i = i+1;
    end
end

i=1;
    for t=t_initial:time_step:t_final
        last_term(i,1) = m*yo*(w^2)*cos(w*t);
        i = i+1;
    end

    first_terms = m.*zdotdot + (abs(z).^n).*zdot*eps + k*z;
    ERROR_array = first_terms - last_term;

    ERROR_total = 0;
    for i=1:length(ERROR_array)
        ERROR_total = ERROR_total + ((ERROR_array(i))^2);
    end

    ERROR = sqrt(ERROR_total);
toc
```

Algorithm B.2. model.m function

```
function ERROR = model (x)
[t_initial,t_final,m,k,n,zl,wc,w,fourier_order,eps,zlyo_range] =
inputs();
yo = zl./zlyo_range;
for ind=1:2:((fourier_order*2)-1)
    a(ind) = x(ind);
    b(ind) = x(ind +1);
end
time_step = 0.001;
t=t_initial:time_step:t_final;
z = zeros(length(t),1);
zdot = zeros(length(t),1);
zdotdot = zeros(length(t),1);
last_term = zeros(length(t),1);

for k=1:fourier_order
    i=1;
    for t=t_initial:time_step:t_final
        z(i) = z(i) + ((a(k)*cos(k*w*t)) +  (b(k)*sin(k*w*t)));
        zdot(i) = zdot(i) + (-a(k)*k*w*sin(k*w*t) +
b(k)*k*w*cos(k*w*t));
        zdotdot(i) = zdotdot(i) + (-a(k)*(k^2)*(k^2)*cos(k*w*t) -
b(k)*(k^2)*(w^2)*sin(k*w*t));
        i = i+1;
    end
end
i=1;
    for t=t_initial:time_step:t_final
        last_term(i,1) = m*yo*(w^2)*cos(w*t);
        i = i+1;
    end
    first_terms = m.*zdotdot + (abs(z).^n).*zdot*eps + k*z;
    ERROR_array = first_terms - last_term;

    ERROR_total = 0;
    for i=1:length(ERROR_array)
        ERROR_total = ERROR_total + ((ERROR_array(i))^2);
    end
    ERROR = sqrt(ERROR_total);
```

Table B.3. inputs.m function

```
function
[t_initial,t_final,m,k,n,zl,wc,w,fourier_order,eps,zlyo_range] =
inputs()
fourier_order = 30;
wc = 1;
zlyo_range=0.5;
eps = 106215;
n = 2;
zl=0.01;
m = 0.02;
k = 120;
wn=sqrt(k/m);
w=wc*wn;
t_initial = (0*pi)/w;
t_final = (4*pi)/w;
```

APPENDIX C: SCRIPTS OF DAMPING PROFILE FINDER

Algorithm C.1. Main function

```
tic
close all
clear all
clc
load('coreData_250RPM.mat');

profileSelection = 2;
speed = 205; %(mm/s)
asil = 1;
array_size = length(cropedData)/4;

% DAMPING PROFILES (IMPORTANT: One profile should be open each time)
switch(profileSelection)
    %Profile 1: Constant Prof (3e-5)
    case 1
        desDamping(1:array_size,1) = 0;
        low = 2100;
        high = 2900;
        desDamping(low:high,1) = 3e-5;

        %Profile 2: Negative Curve Profile
    case 2
        desDamping = zeros(array_size,1);
        low = 2300;
        high = 2700;
        desDataNum = high-low;
        xCor = 0;
        yCor = 4e-5;
        r = 3e-5;

        angleInc = pi/desDataNum;
        ang=-pi:angleInc:0;
        x = r*cos(ang);
        y = r*sin(ang);
        x = x + xCor;
        y = y + yCor;

        desDamping(low:high,1) = y;
end
%%DAMPING PROFILING ENDS

%%%MAIN LOOP STARTS HERE
for turnPlus_2 = 194:5:194
    disp(turnPlus_2)
    for turnPlus_1 = 69:5:69
        for turnZero_0 = 296:5:296

            voltagePlus_2 =
interpolationVoltage(cropedData,turnPlus_2);
            voltagePlus_1 =
interpolationVoltage(cropedData,turnPlus_1);
            voltageZero_0 =
interpolationVoltage(cropedData,turnZero_0);
            voltageMinus_1 = voltagePlus_1;
            voltageMinus_2 =  voltagePlus_2;
```

```matlab
%creating phase shifts for 5kHz 250RPM reading
%%% +2 COIL
            timedVolPlus_2 = zeros(length(voltagePlus_2),1);
            timedVolPlus_2(1:340,1) = 0;
            timedVolPlus_2(341:(length(voltagePlus_2)),1) =
voltagePlus_2(1:length(voltagePlus_2)-340,1);
%%% +1 COIL
            timedVolPlus_1 = zeros(length(voltagePlus_1),1);
            timedVolPlus_1(1:170,1) = 0;
            timedVolPlus_1(171:(length(voltagePlus_1)),1) =
voltagePlus_1(1:length(voltagePlus_1)-170,1);
%%%  0 COIL -->This remanis the same. No shifting required
            timedVolZero_0 = voltageZero_0;
%%% -1 COIL
            timedVolMinus_1 = zeros(length(voltageMinus_1),1);
            timedVolMinus_1(1:length(voltageMinus_1)-170,1) =
voltageMinus_1(171:length(voltageMinus_1),1);
            timedVolMinus_1(4831:5000,1) = 0;
%%% -2 COIL
            timedVolMinus_2 = zeros(length(voltageMinus_2),1);
            timedVolMinus_2(1:length(voltageMinus_2)-340,1) =
voltageMinus_2(341:length(voltageMinus_2),1);
            timedVolMinus_2(4661:5000,1) = 0;
%%%%%%%%%%%%%%%%%time shifting ends%%%%%%%%%%%%%%%

            dampingPlus_2 = calcThetaSquare(speed,timedVolPlus_2);
            dampingPlus_1 = calcThetaSquare(speed,timedVolPlus_1);
            dampingZero_0 = calcThetaSquare(speed,timedVolZero_0);
            dampingMinus_1 = calcThetaSquare(speed,timedVolMinus_1);
            dampingMinus_2 = calcThetaSquare(speed,timedVolMinus_2);

            totalDamping = dampingPlus_2 + dampingPlus_1 +
dampingZero_0 + dampingMinus_1 + dampingMinus_2;

% ADDED BY NT: Range of least squares:
% Indicated by two values low and high
% Both between 1 - 20000

            error = desDamping(low:high) - totalDamping(low:high);
            error = error.^2;
            sumError = sum(error);

            A(asil,1) = turnPlus_2;
            A(asil,2) = turnPlus_1;
            A(asil,3) = turnZero_0;
            A(asil,4) = sumError;
            asil = asil + 1;
        end
    end
end
asil = A(:,4);
[y,i] = min(asil);
clc
disp(A(i,1))
disp(A(i,2))
disp(A(i,3))
disp(A(i,4))
toc

turnPlus_2 =  A(i,1);
turnPlus_1 =  A(i,2);
turnZero_0 =  A(i,3);
turnMinus_1 = turnPlus_1;
turnMinus_2 = turnPlus_2;
speed = 205; %(mm/s) calculated by motor RPM data
```

```matlab
%interpolate voltage profiles by using experimental data
voltagePlus_2 = interpolationVoltage(cropedData,turnPlus_2);
voltagePlus_1 = interpolationVoltage(cropedData,turnPlus_1);
voltageZero_0 = interpolationVoltage(cropedData,turnZero_0);
voltageMinus_1 = interpolationVoltage(cropedData,turnMinus_1);
voltageMinus_2 = interpolationVoltage(cropedData,turnMinus_2);

%%%%%%%%%-creating time shifts for 5kHz 250RPM reading-%%%%%%%%%
%%%PLUS 2 COIL
timedVolPlus_2 = zeros(length(voltagePlus_2),1);
for i=1:340
    timedVolPlus_2(i,1) = 0;
end
j=1;
for i=341:(length(voltagePlus_2))
    timedVolPlus_2(i,1) = voltagePlus_2(j);
j=j+1;
end
%%% PLUS 1 COIL
timedVolPlus_1 = zeros(length(voltagePlus_1),1);
for i=1:170
    timedVolPlus_1(i,1) = 0;
end
j=1;
for i=171:(length(voltagePlus_1))
    timedVolPlus_1(i,1) = voltagePlus_1(j);
j=j+1;
end
%%% ZERO 0 COIL -->This remanis the same. No shifting required
    timedVolZero_0 = voltageZero_0;
%%% MINUS 1 COIL
timedVolMinus_1 = zeros(length(voltageMinus_1),1);
for i=1:length(voltageMinus_1)-170
    timedVolMinus_1(i,1) = voltageMinus_1(i+170);
end
for i=i+1:length(voltageMinus_1)
    timedVolMinus_1(i,1) = 0;
end

%%% MINUS 2 COIL
timedVolMinus_2 = zeros(length(voltageMinus_2),1);
for i=1:length(voltageMinus_2)-340
    timedVolMinus_2(i,1) = voltageMinus_2(i+340);
end
for i=i+1:length(voltageMinus_2)
    timedVolMinus_2(i,1) = 0;
end
%%%%%%%%%%%%%%%%%%%%%-time shifting ends-%%%%%%%%%%%%%%%%%%%%%%%%

%calculate damping for each coil
dampingPlus_2 = calcThetaSquare(speed,timedVolPlus_2);
dampingPlus_1 = calcThetaSquare(speed,timedVolPlus_1);
dampingZero_0 = calcThetaSquare(speed,timedVolZero_0);
dampingMinus_1 = calcThetaSquare(speed,timedVolMinus_1);
dampingMinus_2 = calcThetaSquare(speed,timedVolMinus_2);

%sum up all coils
totalDamping = dampingPlus_2 + dampingPlus_1 + dampingZero_0 +
dampingMinus_1 + dampingMinus_2;

%time and displacement vectors for 5kHz 250RPM readings (for
plotting purposes)
timeVector=-0.4998:0.0002:0.5000;
dispVector = timeVector*205;
```

```matlab
%Rest of the code is plotting
figure(1)
set(0,'DefaultFigureWindowStyle','docked')

subplot(3,1,1)
plot(dispVector,timedVolPlus_2,'k')
hold on
plot(dispVector,timedVolPlus_1,'k')
hold on
plot(dispVector,timedVolZero_0)
hold on
plot(dispVector,timedVolMinus_1,'r')
hold on
plot(dispVector,timedVolMinus_2,'r')
hold off
title('Coil Voltages')
xlabel('Displacement (mm)')

subplot(3,1,2)
plot(dispVector,dampingPlus_2,'k')
hold on
plot(dispVector,dampingPlus_1,'k')
hold on
plot(dispVector,dampingZero_0)
hold on
plot(dispVector,dampingMinus_1,'r')
hold on
plot(dispVector,dampingMinus_2,'r')
hold off
title('Theta Square')
xlabel('Displacement (mm)')

subplot(3,1,3)
plot(dispVector,totalDamping)
hold on
plot(dispVector,desDamping,'r')
title('Theta Square Total')
xlabel('Displacement (mm)')
```

Algorithm C.2. interpolationVoltage.m function

```matlab
function[inter] = interpolationVoltage(cropedData,z)
x = 100;
y = 150;

a = zeros(length(cropedData)/4,1);
b = zeros(length(cropedData)/4,1);

a(1:length(a),1) =
cropedData(length(cropedData)*3/8+1:length(cropedData)*5/8,1);
b(1:length(b),1) =
cropedData(length(cropedData)*3/8+1:length(cropedData)*5/8,2);
inter = (((((b-a)./(y-x))* (y-z))-b)*(-1);

end
```

Algorithm C.3. calcThetaSquare.m function

```
function[thetaSquare] = calcThetaSquare(speed,voltageData)
    thetaSquare = voltageData ./ speed;
    thetaSquare = thetaSquare.^2;
end
```

REFERENCES

1. Bult K et al, "*A distributed, wireless MEMS technology for condition based maintenance Proc. 1996 Integrated Monitoring*", Diagnostics and Failure Prevention Conference, Society of Machine Failure Protection Technology (MPFT) (Mobile, AL, USA) pp 373–80, 1996

2. Beeby S.P., Tudor M.J. and White N.M. "*Energy harvesting vibration sources for microsystem applications*", Measurement Science and Technology, 17:127-195, 2006

3. S. J. Roundy, "*Energy scavenging for wireless sensor nodes with a focus on vibration to electricity conversion*", Ph.D. dissertation, Dept. Mech. Eng., Univ. of California, Berkeley, CA, 2003.

4. Xianzhi et al., "*Energy harvesting from mechanical vibrations using multiple magnetostrictive piezoelectric composite transducers*", Sensors and Actuators A: Physical, 2011

5. Bouendeu E., Greiner A., Smith P.J., Korvink J.G., "*A low cost electromagnetic generator for vibration energy harvesting*", IEEE Sensors Journal, 2011

6. White N.M., Glynne-Jones P., Beeby S.P., "*A novel thick-film piezoelectric micro-generator*", Smart Materials and Structures, 2001

7. D. S. Nguyen, E. Halvorsen, G. U. Jensen, A. Vogl, "*Fabrication and Characterization of a wideband MEMS energy harvester utilizing nonlinear springs*", Journal of Micromechanics and Microengineering 20: pp. 125009, 2010

8. Ramlan R., Brennan M.J., Mace B.R., Kovacic I., "*Potential benefits of nonlinear stiffness in an energy harvesting*", Nonlinear Dynamics, 2009

9. M. Ferrari, *"Improved energy harvesting from wideband vibrations by nonlinear piezoelectric converters"*, Sensors and Actuators A 162: 425-431, 2010

10. Daqaq M.F., *"Response of uni-modal doffing-type harvesters to random forced excitations"*, Journal of Sound and Vibraton, 2010

11. Ferrari M., Ferrari V., Guizzetti M., Marioli D., Taroni A., *"Piezoelectric multifrequency energy converter for power harvesting in autonomous microsystems"*, Sensors and Actuators, 2008

12. Mitcheson P.D., Green T.C., Yeatman E.M., Holmes A.S., "Architectures for vibration-driven micropower generators", Journal of Microelectromechanical Systems, 2004

13. Owens B.A.M., Mann B.P., *"Linear and nonlinear electromagnetic coupling models in vibration based energy harvesting"*, Journal of Sound and Vibrations, 2012

REFERENCES NOT CITED

Philips Batteryless Remote Control Device, http://noughmad.com/2012/01/02/free-harvested-energy/ [Retrieved August 2013]

Hand Shake Flaslight, http://www.okokchina.com/p/ZZ-Other-amping-Utensils/handshake-flashlight--445415.html

"*Format for Theses*", The Institute of Graduate Studies in Science and Engineering, Yeditepe University Press, Istanbul, 2012.

MATLAB, "MATLAB Documentation Center", http://www.mathworks.com/help/matlab/ [Retrieved August 2013]

Wikipedia, "Energy Harvesting", http://en.wikipedia.org/wiki/Energy_harvesting [Retrieved August 2013]

K&J Magnetics Inc, "Properties of Neodymium Magnets", http://www.kjmagnetics.com/specs.asp [Retrieved August 2013]